High-frequency limits of carbon nanotube transistors

by

Li Chen

B.E. (Electrical Engineering), The Wuhan University, 2005

A THESIS SUBMITTED IN PARTIAL FULFILLMENT OF

THE REQUIREMENTS FOR THE DEGREE OF

MASTER OF APPLIED SCIENCE

in

The Faculty of Graduate Studies

(Electrical and Computer Engineering)

THE UNIVERSITY OF BRITISH COLUMBIA

(Vancouver)

October, 2008

Abstract

This thesis is focused on the high-frequency performance of carbon nanotube field-effect transistors (CNFETs). Such transistors show their promising performance in the nanoscale regime where quantum mechanics dominates. The short-circuit, common-source, unity-current-gain frequency f_{T} is analyzed through regional signal-delay theory. An energy-dependent effective-mass feature has been added to an existing Schrödinger-Poisson (SP) solver and used to compare with results from a constant-effective-mass SP solver. At high drain bias, where electron energies considerably higher than the edge of the first conduction sub-band may be encountered, f_{T} for CNFETs is significantly reduced with respect to predictions using a constant effective mass.

The opinion that the band-structure-determined velocity limits the high-frequency performance has been reinforced by performing simulations for *p-i-n* and *n-i-n* CNFETs. This necessitated incorporating band-to-band tunneling into the SP solver. Finally, to help put the results from different CNFETs into perspective, a meaningful comparison between CNFETs with doped-contacts and metallic contacts has been made. Band-to-band tunneling, which is a characteristic feature of *p-i-n* CNFETs, can also occur in *n-i-n* CNFETs, and it reduces the f_{T} dramatically.

Contents

List of Tables

List of Figures

List of Symbols

k Wavevector

z Position along nanotube axis of symmetry

ρ Radial distance from nanotube axis of symmetry

f_T cut-off frequency

χ_t Electron affinity of semiconducting nanotube

ϕ Workfunction

E Energy

E_c Conduction band edge

E_v Valence band edge

E_0 Mid-gap energy level

ψ Wavefunction

q Magnitude of electronic charge

h Planck's constant ($\hbar = \frac{h}{2\pi}$ is Dirac's constant)

ϵ_0 Permittivity of free space

BTBT band-to-band tunneling

DOS density of states

QM quantum mechanics

CEM constant effective mass model

EEM Energy-dependent effective mass model

Acknowledgements

I would like to acknowledge my colleagues Mohammad Ali Mahmoudzadeh and George B. Abadir, for many valuable discussions and comments. I'm grateful to Drs. Leonardo Castro and David John for their patient help and encouragement. I don't think I could have made an impressive achievement without their teaching, especially in the understanding of the Schrödinger-Poisson (SP) solver.

It is with great pleasure and honor that I thank my mentor Professor David Pulfrey, whose profound knowledge and insightful guidance is always a source of inspiration.

Dedication

I want to express my deepest gratitude to John Madden, Anne Coates and Hyoshin Kim, without their kindly suggestions I would not have had the opportunity to come to UBC. Thanks to my friends Michael Lee and Michael Chen who helped me settle in the new environment with many fruitful and interesting discussions. My work would not have been possible without the love and support of my family and friends. They are the inspiration in all of the aspects of my life.

Statement of Co-Authorship

The research presented in the body of this thesis was performed within the UBC Nanoelectronics Group between 2006 and 2008. The simulation code and methods are based on the developments of David L. John and Leonardo C. Castro. This statement describes the author's role in the research reported in this thesis. Chapters 1 and 4 and the Appendices were written by the author. Chapter 2 is a paper with my supervisor that has been accepted for publication. My contribution was to perform the research and prepare the figures for the new results that were added to a review written by my supervisor. Chapter 3 is a paper with my supervisor that has been submitted for publication. I performed the derivations, simulations and analysis; I generated and prepared the figures; I wrote the first draft of the paper, and participated in the collaborative effort that led to the final version of the paper.

Chapter 1

Introduction

The discovery of carbon nanotubes (CNT) by Sumio Iijima in 1991 [1] attracted much attention, from not only fundamental science but also from the perspective of applications. Studies of CNTs have demonstrated their unique nanostructure and remarkable electronic and mechanical properties [2, 3]. An ideal CNT can be considered as a hexagonal web of carbon atoms rolled up to make a seamless hollow cylinder. In 1992, Saito *et al.* proposed a tight-binding model to derive the energy band structure and electronic properties for CNTs [4, 5]. Through different atomic arrangements, CNTs could possess either metallic or semiconducting behaviour. As semiconductors, such one-dimensional nanostructures exhibit a diameter-dependent bandgap and high conductivity.

There are many possible applications for CNTs, such as interconnects [6] and sensors [7]. One of the thrilling possibilities is to build nano-scale transistors, which could be applied for future high-speed VLSI circuits with higher density, and lower power dissipation. The carbon nanotube field-effect transistor (CNFET) employs semiconducting carbon nanotubes as the channel material between two contacts acting as source and drain electrodes, and makes use of the gate voltage to control the essentially one-dimensional transport current [8, 9]. Theoretically, the CNFET could reach a higher frequency domain (terahertz regime) than conventional semiconductor technologies [10], suggesting high-speed wireless applications. In 2006, Chen *et al.* [11] demonstrated a CNFET-based ring oscillator, which is the first complete circuit on one individual CNT [9]. In 2007, Rutherglen and Burke [12] reported successful experimental results for a CNT-based demodulator in an actual AM radio-receiver demodulating high-fidelity music. Although the CNFET has shown some of its potential abilities, the technology, such as fabrication, integration of nanosystems, *etc.* is still in its infancy when compared to state-of-the-art bulk-silicon CMOS devices.

This thesis is a report on the study of the high-frequency capability of single-wall coaxial CNFETs between 2006 and 2008 with the UBC Nanoelectronics Group. Through different types of contact to the CNT channel, three different structures, *n-i-n*, Schottky-barrier (SB) and *p-i-n* CNFETs are investigated and compared. The remainder of this chapter will mention some CNT properties, will cover characteristics relevant to high-frequency performance in short-channel CNFET devices, and will describe the new energy-dependent-effective-mass model, followed by an outline of the thesis.

1.1 Carbon Nanotube

Starting from the nearest neighbour tight-binding approximation, the energy dispersion for graphene (figure 1.1.A) is expressed in the Cartesian coordinate system as:

$$E(k_x, k_y) = \pm\gamma[1 + 4\cos(\frac{\sqrt{3}ak_x}{2})\cos(\frac{ak_y}{2}) + 4cos^2(\frac{ak_y}{2})]^{0.5}, \tag{1.1}$$

where a is the lattice constant and γ is the nearest-neighbour transfer integral [4]. This bandstructure is plotted in figure 1.1.B as a function of wavevectors k_x and k_y. Thus graphene is described as a semi-metal: the valence and conduction bands overlap but only at six points at the corners of the Brillouin zone.

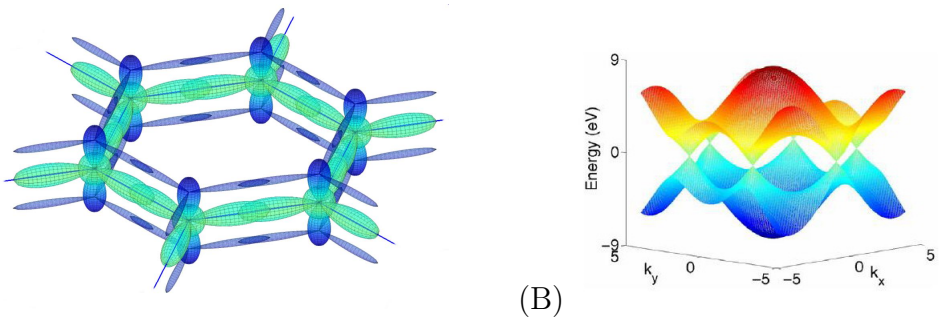

(A) (B)

Figure 1.1: Pictorial representation of: **(A)** Graphene monolayer [13]; and **(B)** Electronic structure [14]

Treating the CNT as a rolled sheet of graphene, first we quantize the wavevector in the circumferential direction:

$$\overrightarrow{k} \bullet \overrightarrow{C} = k_x C_x + k_y C_y = 2\pi p, \tag{1.2}$$

where C is shown in figure 1.2.A and p is an integer. Equation (1.2) indicates that, by rolling the graphene sheet, states in CNT are determined by the particular values of C_x, C_y and p. Therefore electrons are confined in different longitudinal lines intersecting the graphene bandstructure. This could also be the reason that CNTs have less scattering than other semiconducting materials, and that the current transport could be ballistic. Another important property of this formation is that CNTs could be metallic or semiconducting, depending on whether the lines pass through the graphene Fermi points [14].

(A) 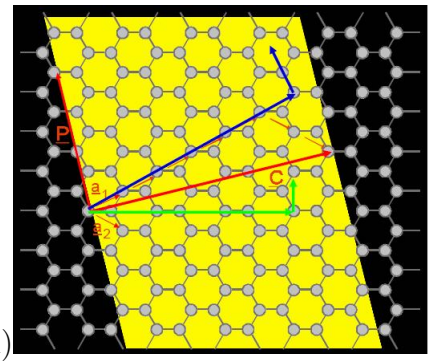

$\longrightarrow$(B) 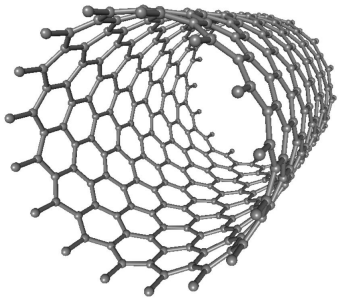

Figure 1.2: Pictorial representation of: (A) Graphene sheet (Courtesy of Richard Martel, IBM); and (B) Single-walled carbon nanotube lattice structures. a_1 and a_2 are the lattice vectors of graphene. $|a_1| = |a_2| = \sqrt{3}a$, where a is the carbon-carbon bond length (Adapted from D.L.John *et al.* [15]).

Substituting k_x, k_y from equation (1.1) with the axial direction wavevector k and C, p components aforementioned, the CNT band structure is expressed by:

$$\begin{aligned} E(k) &= \pm\gamma[1 + 4\ \cos(\frac{3C_x ka}{2C} - \frac{3\pi paC_y}{C^2})\ \cos(\frac{\sqrt{3}C_y ka}{2C} + \frac{\sqrt{3}\pi paC_x}{C^2}) \\ &\quad +4\cos^2(\frac{\sqrt{3}C_y ka}{2C} + \frac{\sqrt{3}\pi paC_x}{C^2})]^{0.5}, \end{aligned} \tag{1.3}$$

where $C_x = a\sqrt{3}(n + 0.5m)$ and $C_y = 1.5am$. The integer sequence (n, m) is called the chirality, which is used to differentiate CNTs. For example, $(n, 0)$ is labelled as a zigzag tube. When $|n - m| = 3 * I$ where I is an integer, the CNT's energy band crosses the Fermi points, and thus it behaves metallically.

From equation (1.3), the propagation velocity of electrons carrying the conduction current, which is also called the band-structure-determined velocity v_b $(=\partial E/\hbar\partial k)$, plays an important role for ballistic FETs in high-frequency performance [16]. The evidence shows the maximum band velocity v_{max} in carbon nanotube channels outperforms other materials in the form of nanocylinders [18].

1.2 Modeling Coaxial CNFETs

Based on the CNT's extraordinary properties, such as high mobility, ultrathin body channel, *etc.,* CNFETs use semiconducting CNTs as the channel material between two electrodes, which are either doped contacts, or metals forming a Schottky barrier. Figure 1.3 depicts the coaxial CNFET structure. A gate completely surrounds the dielectric to reduce short channel effects like drain-induced barrier lowering. Meanwhile, the coaxial geometry maximizes the capacitive coupling between the gate electrode and the nanotube surface, thereby inducing more channel charge at a given bias than other geometries. From a computational point of view, this structure reduces simulation dimensions by one due to its azimuthal symmetry.

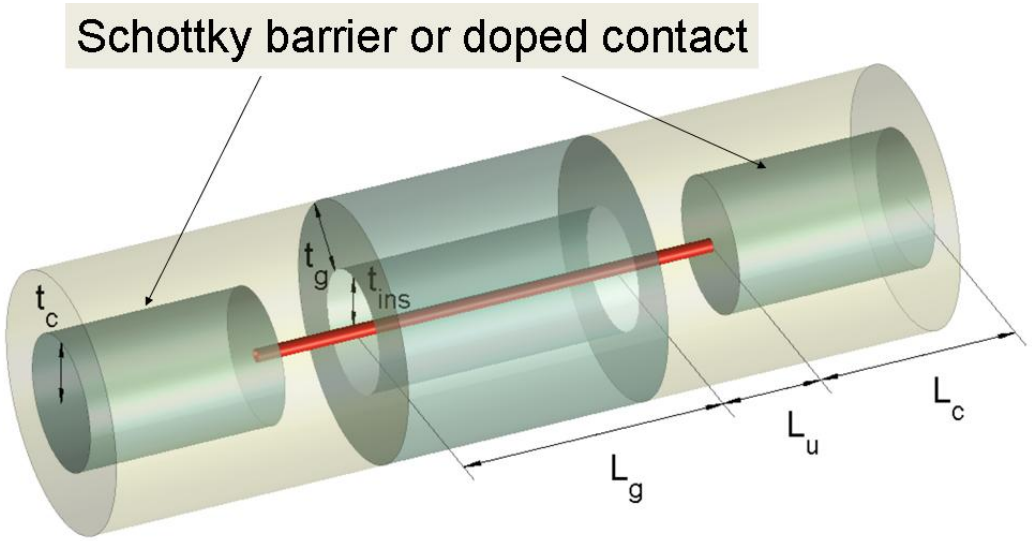

Figure 1.3: Sketch of coaxial CNFET [17]

Work in the UBC Nanoelectronics Group by D. L. John and L. C. Castro has developed a self-consistent Schrödinger-Poisson solver [19], upon which this author's work is based. This thesis introduces an energy-dependent effective mass $m^*(E)$ based on Flietner's work [20], but extends it to apply to the entire band structure, rather than only to the bandgap region. Applying charge-control theory [21] to FETs, the overall, source-drain signal delay time τ_{SD} relates to the unity-current-gain frequency f_T, and to the change in input charge that is required to bring about a change in output current

$$\tau_{SD} = \frac{1}{2\pi f_T} = \frac{\partial Q}{\partial I}. \tag{1.4}$$

For a FET, ∂Q is the change in charge either on the gate or the tube ($\partial Q_G \equiv -\partial Q_{CNT} = \partial Q_{in}$), ∂I is the change in drain current. The signal velocity in the CNFET channel, defined as $v_{sig}(z) = \left[\frac{\partial Q(z)}{\partial I}\right]^{-1}$, does not exceed the highest propagation velocity attained in the drain [16].

1.2.1 Electrostatics

The axial symmetry of the coaxial structure in figure 1.3 reduces the simulation space to 2D, as shown in figure 1.4. Therefore, Poisson Equation in this cylindrical system is expressed as:

$$\frac{\partial^2 V}{\partial^2 \rho} + \left(\frac{1}{\rho} + \frac{1}{\epsilon}\frac{\partial \epsilon}{\partial \rho}\right)\frac{\partial V}{\partial \rho} + \frac{\partial^2 V}{\partial^2 z} = -\frac{Q_v(\rho, z)}{\epsilon}, \tag{1.5}$$

where $V(\rho, z)$ is the potential within the device cylinder, $Q_v(\rho, z)$ is the volumetric charge density, ϵ is the permittivity. Boundary conditions are applied at the interface of each pair of different materials. The Dirichlet boundary conditions on the surface of the source, drain, and gate terminals are given by

$$V(\rho, 0) = -\phi_S/q \tag{1.6}$$

$$V(\rho, L_t) = V_{DS} - \phi_D/q \tag{1.7}$$

$$V(R_g, z) = V_{GS} - \phi_G/q, \tag{1.8}$$

where ϕ is the work function of each electrode, V_{GS} and V_{DS} are the gate- and drain-source voltages, respectively. In the Schottky-barrier CNFET case, the electron barrier height at the source/drain-channel interfaces is:

$$\phi_{Bn} = \phi_M - \chi_{CNT}; \tag{1.9}$$

and the hole barrier height is

$$\phi_{Bp} = E_g - \phi_{Bn}. \tag{1.10}$$

χ_{CNT} is the electron affinity of a CNT with bandgap E_g, and since we are using intrinsic CNTs with symmetric conduction and valence band, its relationship with the workfunction is expressed as:

$$\chi_{CNT} = \phi_{CNT} - E_g/2. \tag{1.11}$$

Due to the discontinuity in permittivity ϵ at the nanotube-insulator and insulator-gate interfaces, a matching condition is applied to the electric flux from Gauss's law:

$$\epsilon_{ins}\frac{\partial V}{\partial \rho}\bigg|_{\rho=R_t^+} - \epsilon_t\frac{\partial V}{\partial \rho}\bigg|_{\rho=R_t^-} = -\frac{q(p-n)}{2\pi R_t \epsilon_0}, \tag{1.12}$$

$$\int_{z_S}^{z_D} r_G\frac{\partial V}{\partial \rho}\bigg|_{\rho=R_t} dz + \int_{r_G}^{r_G+t_g} \rho\frac{\partial V}{\partial z}\bigg|_{z=z_S} d\rho - \int_{r_G}^{r_G+t_g} \rho\frac{\partial V}{\partial z}\bigg|_{z=z_D} d\rho = \frac{Q_G}{2\pi\epsilon_{ins}\epsilon_0}. \tag{1.13}$$

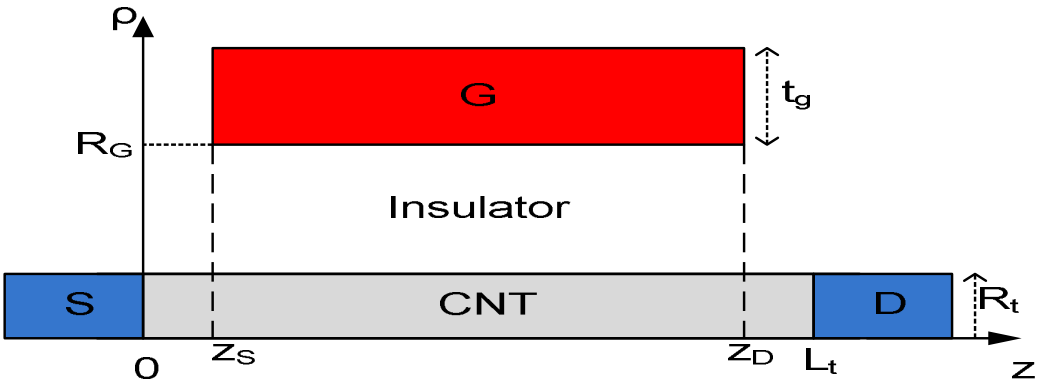

Figure 1.4: 2D simulation space. Axes z and ρ are also shown.

p, n are the hole and electron concentrations respectively, within the CNT circumference at distance z, Q_G is the gate electrode charge, and the relative permittivity of the CNT ϵ_t is one in this work [22]. Since there are no dangling bonds at the CNT surface, there is

less restriction on the choice of dielectric as gate insulator. Various dielectrics have been proposed in the literature, from the usual silicon dioxide ($\epsilon_{ins} \cong 3.9$) [23] to high-κ HfO_2 films ($\epsilon_{ins} \cong 20$) [24].

The fringing electric fields between the gate and other terminals, determined by equation (1.13), induce the parasitic capacitance. This could be comparable to the intrinsic device capacitances, and hence must be considered [10]. A notable example is that an increased gate-metal thickness t_g causing larger parasitic capacitance will reduce CNFET high-frequency performance dramatically [18].

1.2.2 Transport

Because of their molecular uniformity and quasi-one-dimensional nature, carbon nanotubes are expected to have longer electron mean free paths than silicon. Theoretical predictions stated they would be ballsitic for most nanotube diameters encountered in experiments [25]. Electron conduction within the small scale (between 1 and 100 nm) must be treated quantum mechanically to account for QM reflection and tunnelling in the device. The 1D Schrödinger wave equation is employed for the charge on the CNT surface, with Poisson's equation to establish a self-consistent relation between the surface potential $V(R_t^-, z)$ and charge within the CNFET domain.

From the Landauer-Büttiker formalism, the device is treated as being composed of two carrier reservoirs, connected by a 1D scattering region described by a transmission coefficient *T(E)*. Each contact region is described by its own equilibrium carrier statistics $f(E)$, and is assumed to be also one-dimensional. Under this formalism, the electron current $I(E) = -qnv$, where the charge density is

$$n(E) = g(E)f(E)T(E)/2, \tag{1.14}$$

with the density of states accounting for spin-degeneracy $g(E) = (2/\pi)(\partial k/\partial E)$, and the

band-structure-determined velocity is v. Therefore the current can be expressed below:

$$I = -\frac{2q}{h}\int [f(E-\mu_S) - f(E-\mu_D)]T(E)dE. \tag{1.15}$$

μ_S and μ_D are the source and drain Fermi levels, respectively. Note that for each contact only half of the electrons inject into the channel, so either $+k$ or $-k$ modes are considered; This is the reason the division sign appears in the charge density formula Equation (1.14).

The transmission coefficient $T(E)$ is expressed as

$$T(E) = \frac{\psi_D \psi_D^*}{\psi_S \psi_S^*}\frac{v_D}{v_S}, \tag{1.16}$$

where $\psi(E)$ is the electron wavefunction, * denotes the complex conjugate, $v(E)$ is the group velocity and S, D are the source and drain terminals, respectively. From the one-dimensional Schrödinger equation, the wavefunction can be expressed by incident and reflected waves:

$$\psi(z) = a_z e^{ikz} + b_z e^{-ikz}, \tag{1.17}$$

where k are the wavevectors and a_z, b_z are coefficients to be determined. Matching conditions on the boundary x_{ij} between adjacent layers i and j are expressed as:

$$\psi_i(x_{ij}) = \psi_j(x_{ij}), \tag{1.18}$$

$$\frac{1}{m_i^*(E)}\frac{\partial \psi_i}{\partial z}\bigg|_{z=x_{ij}} = \frac{1}{m_j^*(E)}\frac{\partial \psi_j}{\partial z}\bigg|_{z=x_{ij}}. \tag{1.19}$$

Equation (1.19) includes an effective-mass to satisfy current conservation. Use of an energy-dependent effective mass $m^*(E)$ here, and as described in the next section, is the main contribution of this thesis. Details of using a matrix method to solve the Schrödinger equation can be seen in Appendix A.

1.3 Energy-dependent Effective Mass Model (EEM)

Based on Flietner's work [20], the energy-dependent effective mass within any sub-band b can be expressed as:

$$m^*(E) = \frac{m_b}{2\Delta_b}(|E - E_0| + \Delta_b), \tag{1.20}$$

where E_0 is the mid-gap energy level, Δ_b is one-half of the bandgap for sub-band b, and m_b is the constant, parabolic-band, effective mass for sub-band b. Combined with the formula $E = E_c + \frac{\hbar^2 k^2}{2m^*}$ for states above the conduction band, the band-structure-determined velocity $v_{band}(E - E_c)$ is drawn in figure 1.5 for the energy-dependent effective mass model (dashed line). Curves from a tight-binding calculation (TBA - dotted line), in which an overlap parameter of 2.8 eV is used, and constant effective mass (solid line) are also plotted here. The appropriate values for (11,0) tube parameters in equation (1.20) are $m_b = 0.122m_0$, $\Delta_b \equiv (E_c - E_0) = 0.473$ eV. Clearly, the energy-dependent effective-mass approach gives significantly better agreement at higher energies.

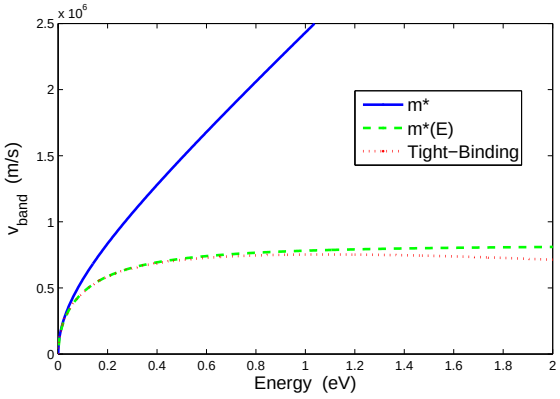

Figure 1.5: Energy dependence of v_{band} for the first sub-band of (11,0) tube

The 1D DOS (density of states) $g(E) = (2/\pi)(\partial k/\partial E)$, can be expressed as a function of

m^* and E above the conduction band:

$$g(E) = \frac{1}{\pi\hbar}\sqrt{\frac{2m^*}{E - E_c}}. \tag{1.21}$$

From equation (1.20), the DOS computed from EEM is larger than CEM. The charge densities can be expressed as:

$$Q(z, E) = q\sum_b D_b[\mathcal{G}_{S,b}(z, E)(u - f_S) + \mathcal{G}_{D,b}(z, E)(u - f_D)], \tag{1.22}$$

where D_b is the degeneracy of sub-band b, $\mathcal{G}_{C,b}$ is the local density of states (LDOS) arising from coupling to contact C , and f_C is the Fermi function at contact C. The actual LDOS is given by the density of states and the wavefunction:

$$\mathcal{G}_{C,b}(z, E) = g_{C,b}(E)\psi_C(z, E)\psi_C^*(z, E) \tag{1.23}$$

The parameter u is used to differentiate between electrons and holes:

$$u(z, E) = \begin{cases} 0, & E > E_0 \quad \text{(electron)} \\ 1, & E < E_0 \quad \text{(hole)}. \end{cases} \tag{1.24}$$

In figure 1.6, the frequency f_T results are presented for a doped-contact *n-i-n* CNFET comprising an (11,0) nanotube in a coaxial structure with the following specifications: gate length 7 nm, gate thickness 0.1 nm, oxide thickness 2 nm, oxide relative permittivity 3.9, source and drain length 30 nm, source and drain doping 0.5 /nm.

In ballistic CNFETs, the electrons comprising the current attain their highest energies as they exit the gated, intrinsic portion of the nanotube, and enter the doped portion of the drain contact [16]. Thus, as the drain-source voltage V_{DS} increases, one would expect to see the constant-effective-mass approach yielding increasingly exaggerated values of v_{band}.

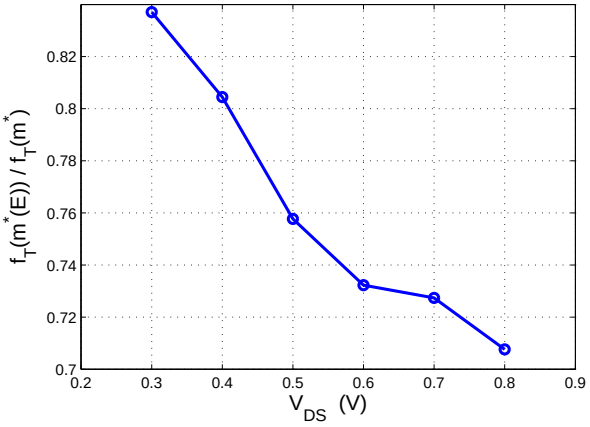

Figure 1.6: Drain-bias dependence of the ratio of f_T for the energy-dependent effective-mass case to that for the constant effective-mass case. $V_{GS} = 0.5\,\mathrm{V}$.

This, in turn, would lead to an increasing underestimate of the contribution of the above-mentioned portion of the nanotube to the signal delay and, consequently, to an overestimate of f_T as V_{DS} increases. Figure 1.6 confirms that this is indeed the case.

One would expect that the switch to $m^*(E)$ from a constant effective mass would lower the transconductance g_m, as this parameter is directly related to the carrier velocity. However, in CNFETs contacted by positive Schottky barriers, g_m has an interesting dependence on gate bias V_{GS} due to internal resonances [26]. The result is shown in figure. 1.7: the peak is shifted and is slightly higher than in the constant-effective-mass case.

g_m is related to current, and higher values are obtained as the bandgap of the nanotube is reduced [27]. The bandgap is inversely related to the diameter and chirality of the nanotube, and it is shown in this thesis (Appendix B) that, for zig-zag tubes, the propagation velocity (band-structure-limited velocity) has a maximum value (for the first sub-band) of $v_{b,max} = 9.1 \times 10^5\,\mathrm{m/s}$ for tubes of chirality ($3i$+1,0), where i is an integer, and a peak value that increases towards $v_{b,max}$ as i increases for tubes of chirality ($3i$+2,0). This behaviour is illustrated in figure 1.8 and more details are given in Appendix B. When this "oscillation" in peak velocity is combined with the improvement in g_m that results from having a lower source/channel barrier height in higher chirality tubes, the f_T-chirality plot

for doped-contact n-i-n CNFETs exhibits the interesting form shown in figure 1.9.

The results presented so far have been for structures with near-zero-thickness gate metal, and for no series resistance in the source and drain contacts. The effects of increasing the gate metal thickness to 10 nm, and of adding some contact resistance to an *n-i-n* CNFET have been examined in this thesis and are shown in figure 1.10. It can be seen that the "headroom" over conventional transistors is not great when these practical features are added to the simulations.

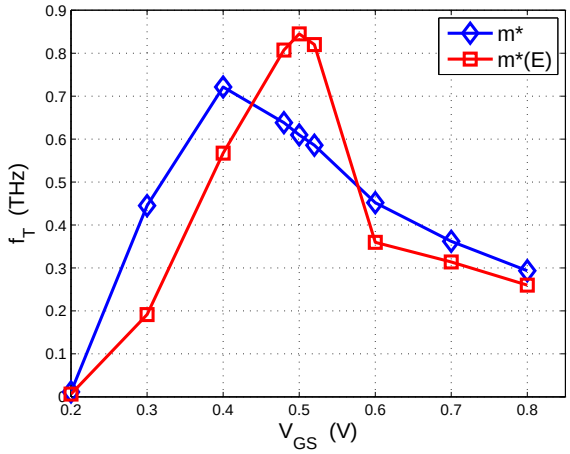

Figure 1.7: Gate-bias dependence of f_T for a SB-CNFET, for constant- and energy-dependent-effective mass. $V_{DS} = 0.5\,\mathrm{V}$, gate length =20 nm.

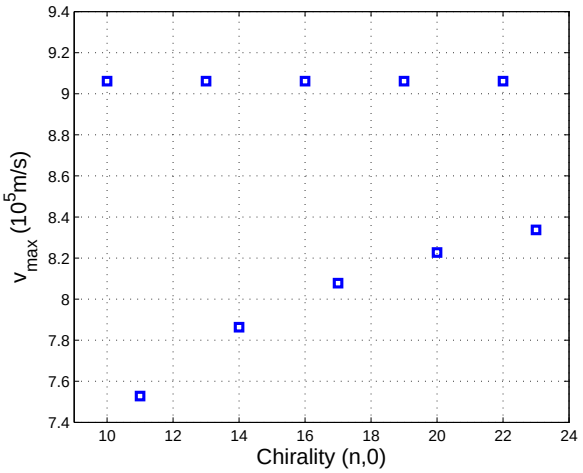

Figure 1.8: Dependence of maximum, band-structure-limited velocity on chirality for zig-zag nanotubes.

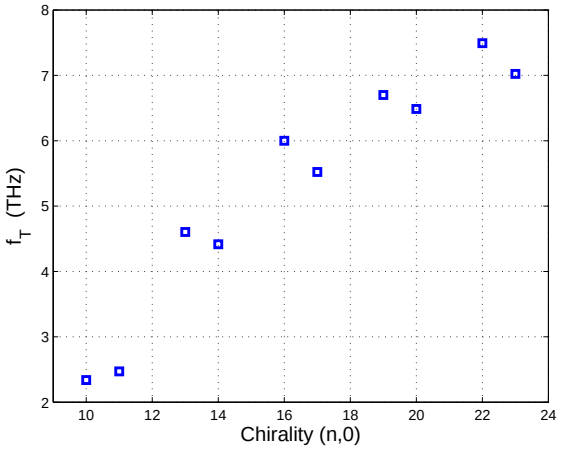

Figure 1.9: f_T dependence on chirality for a n-i-n CNFET. $V_{DS} = 0.7\,\mathrm{V}$, $V_{GS} = 0.5\,\mathrm{V}$, gate length=7 nm.

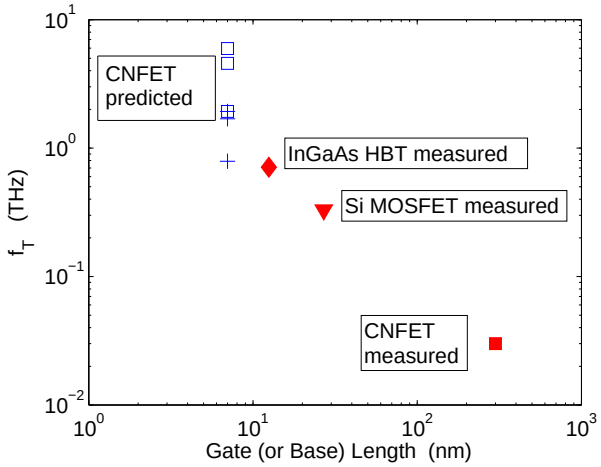

Figure 1.10: Record measured f_T values for various transistors [28–30], and predicted results for n-i-n CNFETs. Open-square data: increasing the gate metal thickness (0.1, 1, 10nm) reduces f_T. Cross data: increasing the contact resistance (0, 5, 50 $k\Omega$) further reduces f_T.

1.4 Thesis Outline

In the following chapters, two manuscripts published in, or submitted to, journals over the course of researching CNFETs are presented, followed by a conclusion summarizing the key achievements and addressing future work. Chapter 2 analyzes the high-frequency performance of CNFETs, using a self-consistent, constant effective-mass Schrödinger-Poisson solver. A meaningful comparison between CNFETs with doped-contacts and metallic contacts has been made. Chapter 3 compares the high-frequency capabilities of *p-i -n* and *n-i-n* doped-contact CNFETs via EEM simulations, and considers the effect of band-to-band tunneling in both devices. Other relevant work performed by the author appears in the appendices. In Appendix A, a detailed matrix method for solving the Schrödinger equation is given. Appendix B derives the first-band velocity formalism for zigzag CNTs from Tight-Binding theory. Appendix C identifies a problem with SP modeling problem

that is facing when including band-to-band tunneling.

1.5 Specific Contributions

The work presented in this thesis has contributed to determining the high-frequency limits of carbon nanotube field-effect transistors. The energy-dependent effective mass model developed here shows its superiority over the constant effective mass method, especially as the drain-source bias is increased. In addition, an in-depth analysis explains how the band-structure -determined velocity of zig-zag carbon nanotubes changes as chirality increases. Such behavior also influences the CNFET's high-frequency performance. Band-to-band tunneling (BTBT) has been incorporated into the model and shown to reduce the performance of n-i-n CNFETs. Also parasitics, in the form of gate metal thickness and contact resistance, have been included to better predict the performance of realistic device structures.

References

[1] S. Iijima, "Helical microtubules of graphitic carbon", Nature, vol. 354, pp. 56–58, 1991.

[2] M. S. Dresselhaus, G. Dresselhaus, and P. C. Eklund, Science of Fullerenes and Carbon Nanotubes (Academic Press, Toronto, 1996).

[3] Mildred S. Dresselhaus, Gene Dresselhaus, and Phaedon Avouris, eds., *Carbon Nanotubes: Synthesis, Structure, Properties, and Applications*, vol. 80 of Topics in Applied Physics (Springer, Berlin, 2001).

[4] R. Saito, M. Fujita, G. Dresselhaus, and M. S. Dresselhaus, "Electronic structure of chiral graphene tubules", Appl. Phys. Lett., vol. 60, pp. 2204–2206, 1992.

[5] R. Saito, M. Fujita, G. Dresselhaus, and M. S. Dresselhaus, "Electronic structure of graphene tubules based on c60", Phys. Rev. B, vol. 46, pp. 1804–1811, 1992.

[6] F. Kreup, A. P. Graham, M. Liebau, G. S. Duesberg, R. Seidel, and E. Unger, "Carbon nanotubes for interconnect applications", in IEDM Tech. Dig., pp. 683–686, 2004.

[7] Liming Dai, Prabhu Soundarrajan, and Taehyung Kim, "Sensors and sensor arrays based on conjugated polymers and carbon nanotubes", Pure Appl. Chem., Vol. 74, No. 9, pp. 1753–1772, 2002.

[8] S. J. Tans, A. R. M. Verschueren, and C. Dekker, "Room-temperature transistor based on a single carbon nanotube", Nature, vol. 393, pp. 49–52, 1998.

[9] J. Appenzeller, "Carbon nanotubes for high performance electronics—Progress and prospect", Proc. IEEE, vol. 96, no. 2, Feb. 2008.

[10] Peter J. Burke, "AC performance of nanoelectronics: towards a ballistic THz nanotube transistor", Solid-State Electronics, Vol. 48, Iss. 10-11, 1981-1986, 2004

[11] Z. Chen, J. Appenzeller, Y.-M. Lin, J.S. Oakley, A.G. Rinzler, J. Tang, S. Wind, P. Solomon, and Ph. Avouris, "An integrated logic circuit assembled on a single carbon nanotube", Science, vol. 311, 1735, 2006.

[12] Chris Rutherglen and Peter Burke, "Carbon Nanotube Radio", Nano Lett., 7(11) pp 3296–3299, 2007.

[13] L.C. Castro, Ph.D. Thesis. The University of British Columbia, 2006.

[14] M P Anantram and F Léonard, "Physics of carbon nanotube electronic devices", Rep. Prog. Phys. 69, 507-561, 2006.

[15] D.L. John, L.C. Castro, P.J.S. Pereira and D.L. Pulfrey, "A Schrödinger-Poisson Solver for Modeling Carbon Nanotube FETs", *Tech. Proc. of the 2004 Nanotechnology Conf. and Trade Show,* vol. 3, pp. 65-68, 2004.

[16] D.L. Pulfrey, L.C. Castro, D.L John, and M. Vaidyanathan, "Regional signal-delay analysis applied to high-frequency carbon nanotube FETs", IEEE Trans. Nanotechnology. vol. 6, 711-717, 2007.

[17] L.C. Castro and D.L. Pulfrey, "Extrapolated fmax for Carbon Nanotube FETs", Nanotechnology, vol. 17, pp. 300-304, 2006.

[18] D.L. Pulfrey and Li Chen, "Examination of the high-frequency capability of carbon nanotube FETs", Solid-State Electronics, vol. 52, 9, pp. 1324-1328, 2008.

[19] D. L. John, L. C. Castro, P. J. S. Pereira, and D. L. Pulfrey, "A Schrödinger-Poisson solver for modeling carbon nanotube FETs", in Tech. Proc. of the 2004 NSTI Nanotechnology Conf. and Trade Show, vol. 3, (Boston, U.S.A.), pp. 65–68, March 2004.

[20] H. Flietner, Phys. Stat. Sol. (b), vol. 54, 201-208, 1972.

[21] H. K. Gummel, "On the definition of the cutoff frequency f_T ", Proc. IEEE, vol. 57, no. 12, p. 2159, Dec. 1969.

[22] F. Leonard and J. Tersoff, "Multiple Functionality in Nanotube Transistors", Physical Review Letters, vol. 88, Jun. 2002, p. 258302.

[23] J.A. Misewich *et al.*, "Electrically Induced Optical Emission from a Carbon Nanotube FET", Science, vol. 300, May. 2003, pp. 783-786.

[24] A. Javey *et al.*, "Carbon Nanotube Field-Effect Transistors with Integrated Ohmic Contacts and High- Gate Dielectrics", Nano Letters, 4 (3), 447 -450, 2004.

[25] C. T. White and T. N. Todorov, "Carbon nanotubes as long ballistic conductors", Nature, 393, 240-242 (1998).

[26] D.L. John, L.C. Castro, and D.L. Pulfrey, "Quantum capacitance in nanoscale device modeling, J. Appl. Phys., vol. 96, 5180-5184, 2004.

[27] D.L. Pulfrey, Proc. IEEE ESSDERC, pp. 234-238, 2007.

[28] W. Hafez, W. Snodgrass, and M. Feng, Appl. Phys. Lett., vol. 87, 252109, 2005.

[29] S. Lee *et al.*, IEDM Tech. Digest, 241-244, 2005.

[30] A. Le Louarn *et al.*, Appl. Phys. Lett., vol. 90, 233108, 2007.

Chapter 2

Examination of the High-frequency Capability of Carbon Nanotube FETs

2.1 Introduction

This invited paper provides an opportunity to update a critique of the high-frequency performance of CNFETs presented at ESSDERC-07 [1]. The focus is on the short-circuit, common-source, unity-current-gain frequency, f_{T}. The existing measured data is collected, and a new record value is reported [2]. The existing simulation results for Schottky-barrier (SB) CNFETs are collected, and grouped such that the effects on f_{T} of the following factors can be clearly seen: oxide permittivity, tube chirality, extrinsic capacitance, contact size and resistance, phonon scattering. New simulation results for doped-contact *n-i-n* CNFETs are added to the data presented in Ref. [1]; they show the effect on f_{T} of: tube chirality, gate length, gate metal thickness, and contact resistance. Importantly, correction of some earlier data, which suggested an extraordinarily high f_{T} capability [3, 4], has been noted [5].

It is now observed that all the simulation results for both SB- and doped-contact-CNFETs fall below the limit imposed by the propagation velocity of electrons in the gated region of the nanotube [6]. This may seem like an obvious result; however, its application to

A version of this chapter has been published. D. L. Pulfrey and Li Chen. "Examination of the high-frequency capability of carbon nanotube FETs", Solid-State Electronics, vol. 52, 9, pp. 1324-1328, 2008.

nanoscale FETs needs to be re-asserted for at least two reasons: firstly, to dispel doubts caused by earlier simulation results [3, 4]; secondly, to re-affirm that "image-charge" effects, which can lead to signal-delay times being shorter than propagation-delay times in field regions of bipolar transistors, are not significant in nanoscale FETs [7], even though a pronounced field can exist in the gated region of doped-contact CNFETs [8].

2.2 Experimental Results

The low current-drive and high input/output impedance of single CNFETs make it difficult to perform direct measurements of high-frequency electrical properties, at least when using instrumentation based on a reference impedance of 50 Ω. In order to make a direct measurement of a recognized high-frequency figure-of-merit, such as f_{T}, it has been realized that CNFETs assembled from multiple nanotubes must be employed [2, 9–11]. Such measurements are in their infancy, and problems of non-parallel nanotubes, the presence of some metallic nanotubes, and excessive gate overlap capacitance need to be addressed. However, progress is being made, and the highest f_{T} recorded thus far, after de-embedding, is 30 GHz [2]. The experimental data is shown in Fig. 2.1; there is some dependence on gate length L_G, which is indicative of the success of the de-embedding procedures employed to negate the effect of the pad parasitics. The figure also shows the gate-length dependence of f_{T}, as predicted in the "ultimate" limit of the signal delay being determined solely by the propagation of electrons through the gated portion of the nanotube [6]. Satisfaction of this condition is equivalent to having no charge change (capacitance) associated either with regions of the CNFET external to the gated-portion, or with parasitic structures. Clearly, such an ideal situation cannot be attained in practice, but the comparison emphasizes that effort should be put into making measurements on structures using shorter nanotubes. Certainly, as Fig. 2.1 also shows, shorter channel lengths or basewidths have been employed to obtain record f_{T} values for other types of transistor: Si MOSFETs (330 GHz [12]) and InP/InGaAs HBTs (710 GHz [13]).

The ultimate limit, referred to above, proposes

$$2\pi f_{\mathrm{T,ultimate}} = \frac{v_{b,\mathrm{high}}}{L_G}\,, \tag{2.1}$$

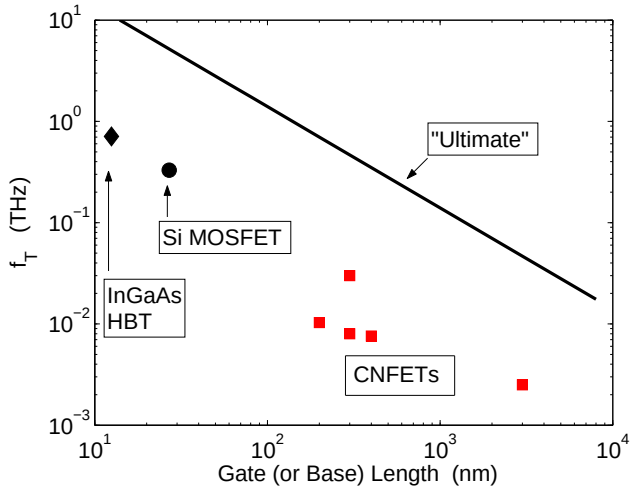

Figure 2.1: Experimental data from high-frequency transistors. CNFETs - squares [2, 9–11]. SiCMOS - circle [12]. HBT - diamond [13]. The "ultimate" curve is from Eq. (2.1).

where $v_{b,\mathrm{high}}$ is the maximum, band-structure-limited velocity that can be attained. In the zig-zag nanotubes considered here, the value of $v_{b,\mathrm{high}}$ depends on the choice of the overlap parameter used in the tight-binding approximation to get the band structure. Here we use 2.8 eV, which gives the maximum velocities listed in Table 2.1 for various tubes. Note that the maximum propagation velocity in the carbon nanotubes is attained around 1 eV above the edge of the first conduction sub-band, and, consequently, is only likely to be reached by electrons injected into a region of high electric field. The "ultimate" line in Fig. 2.1 is drawn for $v_{b,\mathrm{high}} = 8.8 \times 10^5$ m/s: this value gives a convenient figure for $f_{\mathrm{T,ultimate}}$ in THz of $140/L_G$, with L_G in nm. This number is indicative of a fundamental limit, as opposed to a phenomenological limit, for which one proposed value is $80/L_G$ [16].

2.3 Simulation Results

Detailed theoretical analyses involve the self-consistent solution of the equations of Schrödinger and Poisson, usually under the quasi-static approximation [17], which is appropriate as f_{T}

Material	Chirality	Bandgap (eV)	$E_{v_{b,\mathrm{high}}} - E_C$ (eV)	Maximum velocity (10^5 m/s)
C NT	10,0	0.98	1.22	9.1
C NT	11,0	0.95	1.06	7.5
C NT	13,0	0.76	1.11	9.1
C NT	14,0	0.74	1.00	7.9
C NT	16,0	0.62	1.03	9.1
C NT	17,0	0.61	0.96	8.1
C NT	19,0	0.52	0.96	9.1
C NT	20,0	0.51	0.89	8.2
C NT	22,0	0.45	0.90	9.1
Si NW		2.85	≈ 0.6	≈ 5.8
InAs NW		0.48	≈ 0.18	≈ 4.5

Table 2.1: Maximum band-structure-limited velocity, and the energy above the edge of the first conduction sub-band at which it is attained. The Si data is for a [100] nanowire of diameter 1.36 nm, as inferred from data in Ref. [14]. The InAs data is for a [100] nanoribbon of cross-section $13\times13\,\mathrm{nm}^2$, as inferred from data in [15].

is a parameter attained by extrapolation from lower frequencies. Methods involving either an effective-mass wave equation, or a Hamiltonian based on atomistic considerations, have been employed, and, under suitably low-bias conditions, should give similar results [18], provided the simulation space is properly bounded [19].

The extrapolated f_T is given by

$$2\pi f_\mathrm{T} = \frac{\partial I_D}{\partial Q_G} \equiv \frac{g_m}{C_{Gi} + C_{Ge}}\,, \tag{2.2}$$

where ∂I_D and ∂Q_G are changes in output (drain) current and input (gate) charge, respectively, due to a change in gate-source voltage, for example; g_m is the transconductance, and C_{Gi} and C_{Ge} are contributions to the total gate capacitance C_{GG} arising from the region under the gate (intrinsic), and the gate-electrode regions (extrinsic), respectively.

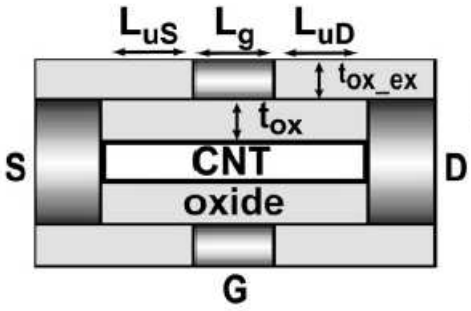

Figure 2.2: Coaxial Schottky-barrier CNFET with wrap-around gate, showing some of the pertinent structural parameters [20].

2.3.1 Schottky-barrier CNFETs

Fig. 2.2 is illustrative of the coaxial, all-around-gate structure that is usually used in simulations of SB-CNFETs [20]. The results that have been obtained for simulation of SB-CNFETs are collected together in Fig. 2.3. The data labeled C_{Ge} comes from two devices of different gate length and underlaps [20, 21]: for the $L_G = 2\,\text{nm}$ case (solid diamonds), the effect is large because of the small gate-source underlap L_{uS} (14 nm); in the $L_G = 5\,\text{nm}$ case (open diamonds), increasing the separation of source and drain electrodes (L_{uS} and L_{uD}) to 24 nm mitigates the effect. The results shown are for contact radii varying from that of the nanotube itself, to that of the nanotube plus oxide and gate thicknesses [21]. The beneficial effect of increasing L_{uD} (from 5 to 25 nm) is also shown by the solid-circle data at $L_G = 50\,\text{nm}$ [25]. The open-circle data at $L_G = 50\,\text{nm}$ comes from a planar structure [24]; the degradation of f_T is again related to an increase in C_{Ge}, and is due to changing the contact from that of a needle of radius equal to that of the nanotube, to that of a metallic strip of width $8\,\mu$m. The latter was the actual electrode structure of a high-performance DC device [27], and emphasizes the need to develop finer contact arrangements for HF devices. It is clear that C_{Ge} has a large effect on the performance of these nanoscale transistors, and it must be included in simulations if predictions of f_T are to be meaningful [28].

The square data points at $L_G = 2\,\text{nm}$ show the effect of increasing ϵ_{ox} from 3.9 to 25 while

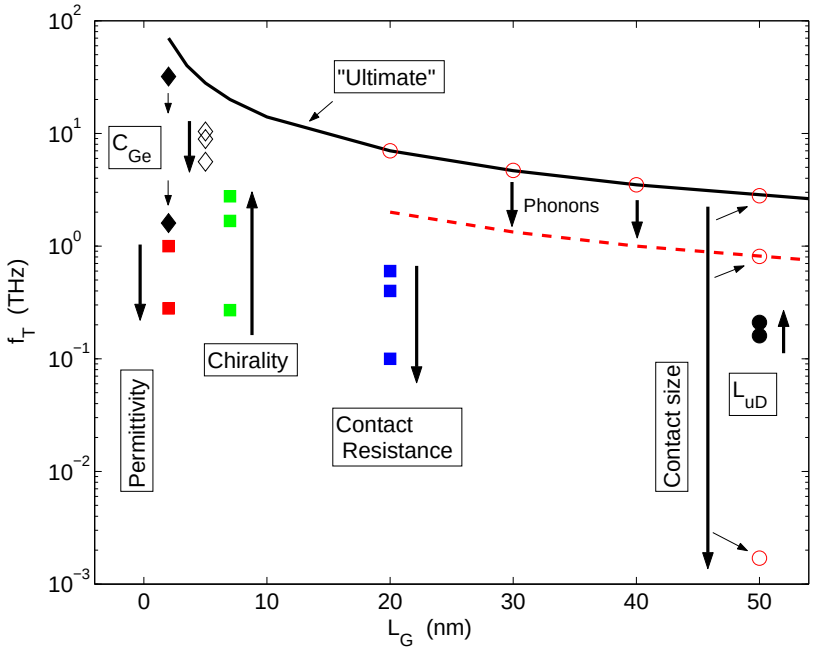

Figure 2.3: Summary of simulation results for SB-CNFETs. Effect of various parameters on f_{T}: C_{Ge} [20, 21]; oxide permittivity and nanotube chirality [22]; contact resistance [23]; contact size [24]; gate-drain underlap [25]; phonon scattering [26]. Arrows indicate increasing parameter.

keeping the insulator thickness fixed at 2.5 nm [22]. The point of these two simulations was to assess the trade-off between increased C_{Gi} (there were no underlaps) and increased g_m due to the stronger electrostatic coupling between gate and nanotube. Evidently, the effect of the capacitance is greater, so f_{T} decreased. For Schottky-barrier contacts representing palladium, the barrier height for hole injection decreases as the nanotube chirality (and diameter) increases [29]. This enhances g_m, leading to the improved performance shown in Fig. 2.3 on changing the chirality from (11,0) (diameter=0.8 nm) through (16,0) to (22,0) (diameter=1.7 nm) [22]. Fig. 2.3 also shows the effect of considering the actual resistance of the source and drain contacts. Such resistances can be expected to be high when employing nanoscale needle contacts. The results shown are for R_{contact} increasing from zero through 10 kΩ to 100 kΩ [23]. Similar degradations also apply to f_{max} [30]. Phonon scattering could be important, at least in tubes of length greater than about 10-20 nm, which is the mean-free-path for optical phonons [26]. The effect is illustrated by the downward shift of the "ultimate" line to that of the dashed line shown in Fig. 2.3 [26]. Phonon scattering leads to a build-up of charge in the channel, *i.e.*, to an increase in C_{Gi}.

2.3.2 Doped-contact CNFETs

In addition to coaxial structures akin to those in Fig. 2.2, double-gate structures, of the form shown in Fig. 2.4 [3, 4], have been used in the simulation of doped-contact-CNFETs. The results that have been obtained for simulation of doped-contact-CNFETs are collected together in Fig. 2.5. Earlier, very high, f_{T} results for double-gate structures [3, 4] have now been corrected [5], bringing them into good agreement with results from other workers [31]. All data shown are for (11,0) nanotubes. Results for a coaxial geometry using the same tube are also shown in Fig. 2.5 [32]. The slightly inferior performance of the coaxial devices is due principally to the increased capacitance that results from this geometrical arrangement. The beneficial effect of increasing the chirality (from (11,0) through (16,0) to (22,0), see the diamond data points) is due to the associated reduction in bandgap (see Table 2.1), which lowers the potential barrier at the doped-source/intrinsic-gated-region interface, thereby improving the transconductance.

Most simulations are performed with an essentially zero-thickness gate electrode. This is convenient from a numerical analysis point-of-view; it reduces the simulation space required

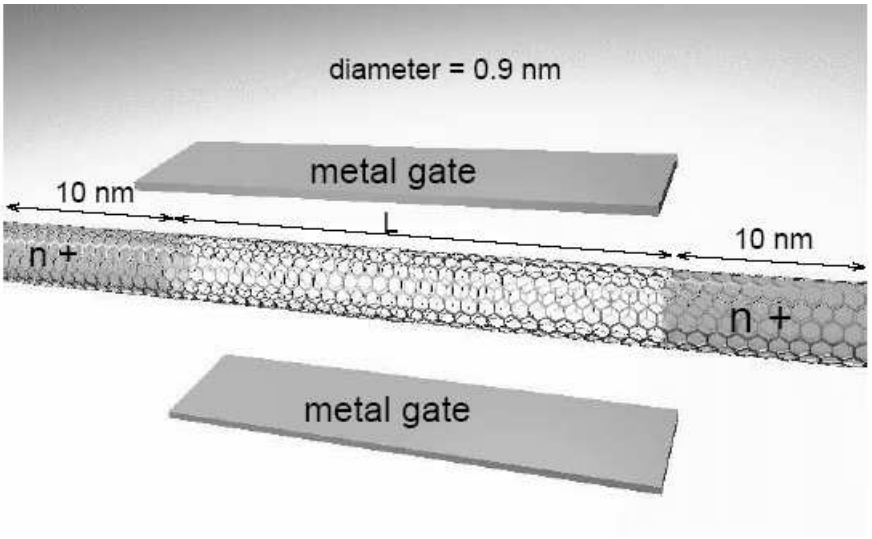

Figure 2.4: Doped-contact CNFET with double-gate [3, 4].

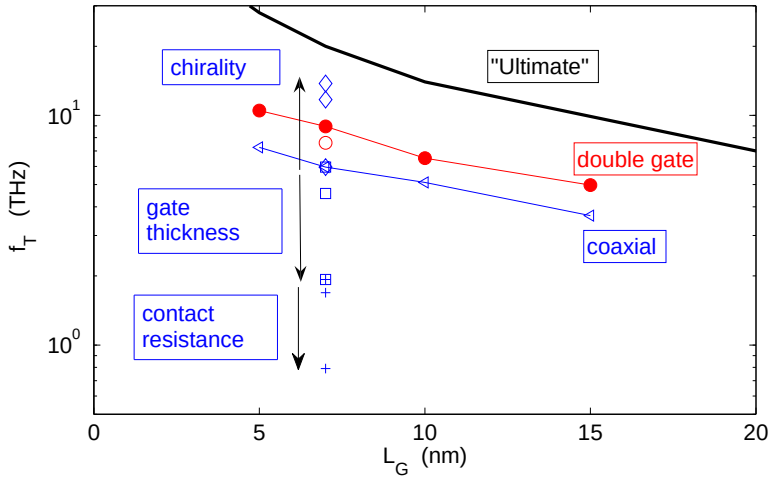

Figure 2.5: Summary of simulation results for doped-contact-CNFETs. Double-gate devices: filled circles [5], open circle [31]. Coaxial devices - diamonds, squares, triangles, crosses [32].

to contain source and drain contacts that are sufficiently long to ensure charge neutrality at their ends [33]. However, it is an unrealistic situation, which is also impractical from the point of view of obtaining a high $f_{\max}$ [30]. Fig. 2.5 (square data points) shows the effect of increasing the gate metal thickness from 0.1 nm through 1 nm to 10 nm. Even though the last value may still be low for a practical device, it does indicate the deleterious effect of the associated increase in C_{Ge}. If a finite contact resistance is added to this, f_{T} is further reduced: Fig. 2.5 (cross data points) shows the effect of 5 and 50 $k\Omega$ of resistance in the source and drain contacts. The latter may not be unreasonable for nanoscale contacts, and it would bring the estimated value of f_{T} down to levels that have actually been realized in another type of transistor [13].

The importance of the gate-metal thickness is emphasized in Fig. 2.6, which breaks down the overall source-drain signal delay τ_{SD} into regional delays [8]

$$\tau_{SD} = \sum_{r}^{L_{CNQ}} \tau_r = \frac{1}{\partial I} \sum_{r}^{L_{CNQ}} \int_r \partial Q(z)\, dz\,, \tag{2.3}$$

where L_{CNQ} is the length of the nanotube over which there is a change in charge, $\partial Q(z)$ is the change in local charge density integrated over energy, and ∂I is the change in drain current. Fig. 2.6 indicates how L_{CNQ} is much enlarged by increasing the gate-metal thickness.

2.3.3 Comparison of Doped-contact- and SB-CNFETs

Fig. 2.3 and Fig. 2.5 display, to the best of our knowledge, all the simulation results that have been reported thus far for f_{T} in CNFETs. However, a comparison between SB- and doped-contact-devices is not easily made from this collection because of the differing device properties that have been used, *e.g.*, device chirality, oxide thickness, voltage bias, and because of the different simulators that have been employed. To provide a meaningful comparison, we provide Fig. 2.7 and Table 2.2, which compare the salient high-frequency parameters for the two types of CNFET with common parameters of: chirality (19,0), L_G = 7 nm, gate-metal thickness = 5 nm, oxide thickness = 2 nm, source/drain underlap = 5 nm, contact lengths = 45 nm, $|V_{GS}| = 0.6$ V, $|V_{DS}| = 0.7$ V. The SB-CNFET used Pd contacts,

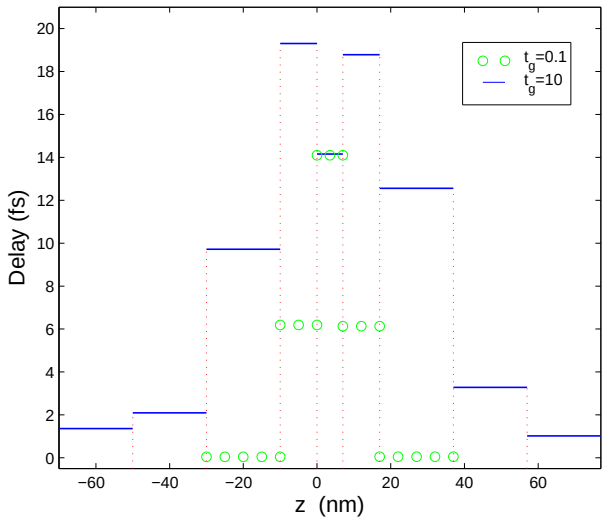

Figure 2.6: Regional signal delay for doped-contact n-i-n CNFETs with gate-metal thicknesses of either 0.1 or 10 nm. In each case the gate is centrally located and $L_G = 7$ nm. Other common parameters are: chirality (11,0), oxide thickness=2 nm, source and drain contacts=70 nm.

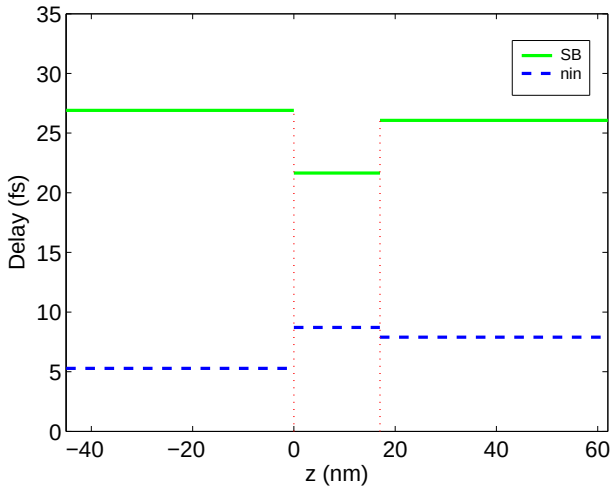

Figure 2.7: Comparison of regional signal delays for SB- and doped-contact-CNFETs with properties described in the text.

whereas the doping density in the doped-contact case was 5×10^8 /m. The parameter values were chosen in accordance with realizing good high-frequency performance. Note that different parameter values would be needed for a CNFET more suited to high-speed digital-logic applications [34, 35], in particular: higher bandgap to produce a reasonable ON/OFF-current ratio, and a longer gate length to reduce source-drain tunneling.

The Table highlights the significant difference in transconductance between the two devices; this is due to the reduced quantum-mechanical reflection of electrons at the injecting source/intrinsic-nanotube interface. The capacitances are only slightly higher in the SB case, but, when taken together with the lower current, of which the lower g_m is a manifestation, they result in significantly higher regional signal delays, as Fig. 2.7 shows.

2.4 Discussion

All of the data presented in this review now falls below the "ultimate" propagation limit [6]. This should now remove speculation about how extraordinarily high values of f_T might

Contacts	g_m (μS)	C_{GG} (aF)	f_{T} (THz)	g_{ds} (μS)	C_{GD} (aF)	R_c ($k\Omega$)	"Extrinsic" f_{T} (THz)
Pd	19.6	1.47	2.1	1.80	0.66	50	1.0
C (n-type)	59.5	1.37	6.9	0.97	0.54	50	2.0

Table 2.2: Comparison of small-signal parameters of SB- and doped-contact-CNFETs having the properties listed in the text. C_{GG} is the total gate capacitance, C_{GD} is the gate capacitance due to a change in V_{DS}, g_{ds} is the drain conductance, R_c is the resistance of each of the source and drain contacts. The extrinsic f_{T} is computed from Ref. [30].

arise in nanoscale FETs due to fortuitous variations in local charge densities [1, 8]. The possibility of the propagation velocity in regions of high field, such as can exist in the channel of short FETs, being exceeded by the signal velocity has also been ruled out [7]. Essentially, this is because any local changes in charge in the nanotube are imaged on the gate electrode, thereby contributing wholly to the change in input charge. The near one-to-one correspondence of nanotube charge and gate charge arises because of the two-dimensional geometry and the close proximity of the gate electrode to the nanotube. In a bipolar transistor, which is essentially a one-dimensional device, the electrostatics is much simpler, and it is easily shown that not all of the charge change within the semiconducting regions is imaged on the input electrode (the base) [36]. This can lead to the signal delay in the base-collector space-charge region being less than the propagation delay in that region.

Inevitably, when considering the performance of a new field-effect transistor, comparisons will be made with Si MOSFETs. This review has suggested that the signal delay in the non-neutral regions of FETs is unlikely to be less than the band-limited propagation delay. Thus, a relevant question is: how does the band-limited propagation velocity v_{band} for carbon nanotubes compare with that in nanoscale Si structures? The result quoted in Table 2.1 suggests that carbon nanotubes have a slight advantage as regards the maximum value of v_{band}, at least when compared to the particular Si nanowire cited. Guo *et al.* have suggested that v_{band} for an ultra-thin body Si MOSFET is about 50% of that in a CNFET [24]. Thus, the ultimate f_{T} in CNFETs would appear to be only slightly greater than might be achievable with nanoscale Si FETs.

These comparisons are for ballistic transport, and it may be argued that attainment of ballistic transport is more likely in a CNFET than in a Si MOSFET, primarily because of the relatively long mean-free-path associated with phonon scattering in carbon nanotubes, but also because of the more one-dimensional form of a tube, as opposed to that of a wire or a ribbon. However, it seems unreasonable to ignore the effect of surface scattering, which greatly affects the mobility in present Si MOSFETs. The nature of the oxide/semiconductor interface is different in the two devices, of course, but some penetration of the electron wavefunctions into the oxide of a CNFET is to be expected. There is presently no information on this, to the authors' knowledge.

We have shown that when the practical features of gate-metal thickness and contact resistance are included in the simulations, then f_{T} for CNFETs can drop into the region of 700-800 GHz. This is about a factor of 2 higher than values that have actually been realized already in planar Si MOSFETs [12]. Add this fact to the need to arrange CNFETs in parallel to improve the current drive, and one wonders whether the small material superiority of v_{band} and the geometrical superiorities of a wrap-around gate and a one-dimensional structure, will be enough to combat the matchless technological superiority of silicon FET processing. Perhaps further research and development in high-frequency CNFETs should be directed towards biological applications, for which silicon-based electronics may be less compatible?

2.5 Conclusions

From this review of the high-frequency performance of CNFETs it can be concluded that:

- experimental f_{T} values should improve by employing multiple, parallel nanotubes of shorter length than used hitherto;
- theoretically, the effects on f_{T} of nanotube chirality (diameter), oxide permittivity, gate-source and gate-drain underlap, source- and drain-electrode diameter and resistance, gate-metal thickness, and phonon scattering are well understood;

- doped-contact CNFETs offer better performance capability than Schottky-barrier devices because of their superior transconductance;
- the presently available simulation data indicates that the signal delay time is not less than the propagation time. This suggests that the band-structure-determined velocity is a key factor in assessing the high-frequency prospects for a FET material. The slight advantage that a carbon nanotube has over silicon in this regard may not be sufficient to offset the technological superiority of Si FETs when it comes to processing practical devices.

Acknowledgement

The authors gratefully acknowledge the profound contributions made to the UBC Nanoelectronics Group by Drs. Leonardo Castro and David John. Financial support was from the Natural Sciences and Engineering research Council of Canada.

References

[1] Pulfrey DL. Critique of high-frequency performance of carbon nanotube FETs. Proc IEEE ESSDERC 2007;234-8.

[2] Le Louarn A, Kapche F, Bethoux J-M, Happy H, Dambrine G, Derycke V, *et al.*. Intrinsic current gain cutoff frequency of 30 GHz with carbon nanotube transistors. Appl Phys Lett 2007;90:233108.

[3] Fiori G, Iannaccone G, and Klimeck G. Performance of carbon nanotube field-effect transistors with doped source and drain extensions and arbitrary geometry. IEDM Tech Digest 2005;522-5.

[4] Fiori G, Iannaccone G, and Klimeck G. A three-dimensional simulation study of the performance of carbon nanotube field-effect transistors with doped reservoirs and realistic geometry. IEEE Trans Elec Dev 2006;53:1782-8.

[5] Fiori G. Private communication. Aug. 29, 2007.

[6] Hasan S, Salahuddin S, Vaidyanathan M, and Alam MA. High-frequency performance projections for ballistic carbon-nanotube transistors. IEEE Trans Nanotechnol 2006;5:14-22.

[7] John DL. Limits to the Signal Delay in Ballistic, Nanoscale Transistors: Semi-Classical and Quantum Results. IEEE Trans Nanotechnol 2008;7:48-55.

[8] Pulfrey DL, Castro LC, John DL, and Vaidyanathan M. Regional signal-delay analysis applied to high-frequency carbon nanotube FETs. IEEE Trans Nanotechnol 2007;6:711-7.

[9] Kim S, Choi T-Y, Rabieirad L, Jeon J-H, Shim M, and Mohammadi S. A poly-Si gate carbon nanotube field-effect transistor for high-frequency applications. Proc IEEE MTT Symp 2005;303-6.

[10] Bethoux J-M, Happy H, Dambrine G, Derycke V, Goffman M, and Bourgoin J-P, An 8-GHz f_T carbon nanotube field-effect transistor for gigahertz range applications. IEEE Electron Dev Lett 2006;27:681-3.

[11] Narita K, Hongo H, Ishida M, and Nihey F. High-frequency performance of multiple-channel carbon nanotube transistors. Physica Stat Sol A 2007;204:1808-13.

[12] Lee S, Jagannathan, Csutak S, Pekarik J, Zamdmer N, *et al.*, Record RF performance of sub-46 nm NFETs in microprocessor SOI CMOS technologies. IEDM Tech Digest 2005;241-4.

[13] Hafez W, Snodgrass W, and Feng M. "12.5 nm base pseudomorphic heterojunction bipolar transistors achieving f_{T}=710 GHz and $f_{\max}$ = 340 GHz. Appl Phys Lett 2005;87:252109.

[14] Wang J, Rahman A, Ghosh A, Klimeck G, and Lundstrom M. Performance evaluation of ballistic silicon nanowire transistors with atomic-basis dispersion relations. Appl Phys Lett 2005;86:093113.

[15] Persson MP and Xu HQ. Electronic structure of [100]-oriented free-standing InAs and InP nanowires with square and rectangular cross sections. Phys Rev B 2006;73:125346.

[16] Burke PJ. AC performance of nanoelectronics: Towards a ballistic THz nanotube transistor. Solid-State Elec 2004;48:1981-6.

[17] Castro LC, John DL, Pulfrey DL, Pourfath M, Gehring A, and Kosina H. Method for predicting f_{T} for carbon nanotube FETs. IEEE Trans Nanotechnol 2005;4:699-704.

[18] Koswatta SO, Neophytou N, Kienle D, Fiori G, and Lundstrom MS. Dependence of DC characteristics of CNT MOSFETs on bandstructure models. IEEE Trans Nanotechnol 2006;5:368-72.

[19] McGuire DL and Pulfrey DL. Error analysis of boundary-condition approximations in the modeling of coaxially gated carbon nanotube FETs. Physica Stat Sol A 2006;203:1111-6.

[20] Alam K and Lake R. Performance of 2 nm gate length carbon nanotube field-effect transistors with source/drain underlaps. Appl Phys Lett 2005;87:073104.

[21] Alam K and Lake R. Dielectric sensitivity of a zero Schottky-barrier, 5 nm gate, carbon nanotube field-effect transistor with source/drain underlaps. J Appl Phys 2006;100:024317.

[22] Castro LC. Unpublished data.

[23] Castro LC, Pulfrey DL, and John DL. High-frequency capability of Schottky-barrier carbon nanotube FETs. Solid-State Phenomena 2007;121-3:693-6.

[24] Guo J, Hasan S, Javey A, Bosman G, and M. Lundstrom. Assessment of high-frequency performance of carbon nanotube FETs. IEEE Trans Nanotechnol 2005;4:715-21.

[25] Pourfath M, Kosina H, Cheong BH, Park WJ, and Selberherr S. Improving DC and AC characteristics of ohmic contact carbon nanotube field-effect transistors. Proc ESSDERC 2005;541-4.

[26] Yoon Y, Ouyang Y, and Guo J. Effect of phonon scattering on intrinsic delay and cut off frequency of carbon nanotube FETs. IEEE Trans Elec Dev 2206;53:2467-70.

[27] Javey A, Guo J, Farmer DB, Wong Q, Yenilnez E, Gordon RG, *et al.*. Self-aligned ballistic molecular transistors and electrically parallel nanotube arrays. Nano Lett 2004;4:1319-22.

[28] Paul BC, Fujita S, Okajima M, and Lee T. Impact of geometry-dependent parasitic capacitances on the performance of CNFET circuits. IEEE Electron Dev Lett 2006;27:380-2.

[29] Chen Z, Appenzeller J, Knoch J, Lin Y-M, and Avouris P. The role of metal-nanotube contact in the performance of carbon nanotube field-effect transistors. Nano Lett 2005;5:1497-502.

[30] Castro LC and Pulfrey DL. Extrapolated $f_{\max}$ for carbon nanotube FETs. Nanotechnology 2006;17:300-4.

[31] John DL, Pulfrey DL, Castro LC, and Vaidyanathan M. Terahertz carbon nanotube FETs: feasible or fantastical?. Proc. 31st WOCSDICE 2007; ISBN: 978-88-6129-088-4.

[32] Chen Li. Unpublished data.

[33] John DL and Pulfrey DL. Issues in the modeling of carbon nanotube FETs: structure, gate thickness and azimuthal asymmetry. J Computational Electronics 2007;6:175-8.

[34] Pulfrey DL, John DL, and Castro LC. Proc 13th Int Workshop Phys Semiconductor Dev 2005;7-13.

[35] John DL and Pulfrey DL, Switching-speed calculations for Schottky-barrier carbon nanotube field-effect transistors. J Vac Sci Tech A 2006;24:708-12.

[36] Laux SE and Lee W. Collector signal delay in the presence of velocity overshoot. IEEE Elec Dev Lett 1990;11:174-6.

Chapter 3

Comparison of p-i-n and n-i-n Carbon Nanotube FETs Regarding High-frequency Performance

3.1 Introduction

Aggressively scaled nanowire and nanotube FETs with isotypically doped source and drain regions are predicted to exhibit large sub-threshold currents, which result from unwanted band-to-band tunneling (BTBT) at the drain end of the device [1, 2]. Contrarily, by using differently doped contacts, *i.e.*, a *p*-type source and an *n*-type drain, BTBT can apparently be exploited to yield inverse sub-threshold slopes below the thermionic-emission limit of 60 mV/decade [3]. However, a possible drawback to such *p*-*i*-*n* tunnel FETs is the reduction in ON current with respect to conventional FETs, in which charge injection is by thermionic emission, rather than tunneling, is the operative injection mechanism [4]. Nevertheless, high ON/OFF current ratios have been predicted, which, coupled with a low switching energy, have led to suggestions that tunnel FETs may be suited to ultra-low power applications [4, 5]. These attributes depend on the suppression of direct source-drain tunneling, either by keeping the channel length above about 15 nm, or by limiting the drain-source bias. The desirable properties of tunnel MOSFETs have led them to be investigated in other semiconductor-material systems [6].

A version of this chapter has been submitted for publication. Li Chen and D.L. Pulfrey, "Comparison of p-i-n and n-i-n carbon nanotube FETs regarding high-frequency performance", Solid-State Electronics, submitted, 8/14/2008.

Here, we explore the capability of *p-i-n* CNFETs for high frequency performance. A comparison with *n-i-n* CNFET*s,* for which we include the BTBT effect, is also given. An energy-dependent effective-mass (EEM) model, rather than a constant effective-mass (CEM) model, is applied to our Schrödinger-Poisson solver [7], thereby allowing achievement of more accurate simulation results for devices in which high electric fields are expected to be present. This situation is likely to arise in the drain region of the device at high drain-source bias and, if not correctly treated, could lead to an underestimate of the signal delay time in this region [11], and to a corresponding overestimate of f_T. We also explore the effect of chirality, thereby extending the work on *n-i-n* CNFETs that has been presented recently [8].

3.2 Method

3.2.1 Energy-dependent Effective-mass Model (EEM)

Flietner's energy-dependent effective-mass formulation is extended to apply to energies within the bands of a carbon nanotube, rather than merely to energies within the bandgap [9]. We write:

$$m^*(E) = \frac{m_b}{2\Delta_b}(|E - E_0| + \Delta_b)\,, \tag{3.1}$$

where E_0 is the mid-gap energy level, Δ_b is one-half of the bandgap for sub-band b, and m_b is a constant, parabolic-band, effective mass for sub-band b.

In our scattering-matrix solution to compute transmission probability [10], the boundary conditions for the derivative of the wavefunction need to include $m^*(E)$ to satisfy current conservation:

$$\frac{1}{m_i^*(E)}\frac{\partial\psi_i}{\partial x}\bigg|_{x=x_{ij}} = \frac{1}{m_j^*(E)}\frac{\partial\psi_j}{\partial x}\bigg|_{x=x_{ij}}\,, \tag{3.2}$$

where x_{ij} is the position of the interface between piece-wise rectangular layers i and j .

The wavevector in the nanotube is given by:

$$k = \sqrt{2m^*(E)(|E - E_0| - \Delta_b)}/\hbar\,. \tag{3.3}$$

The charge densities can by expressed as:

$$Q(z, E) = q \sum_b D_b[\mathcal{G}_{S,b}(z, E)(u - f_S) + \mathcal{G}_{D,b}(z, E)(u - f_D)]\,, \tag{3.4}$$

where D_b is the degeneracy of sub-band b, $\mathcal{G}_{C,b}$ is the local density of states arising from coupling to contact C [11], and f_C is the Fermi function at contact C. The parameter u is used to differentiate between electrons and holes:

$$u(z, E) = \begin{cases} 0, & E > E_0 \quad \text{(electron)} \\ 1, & E < E_0 \quad \text{(hole)}. \end{cases} \tag{3.5}$$

3.2.2 Maximum Band Velocity v_{max} for Zigzag CNTs

In view of the importance of the band-limited velocity in determining the upper-bound to f_T in FETs [12], we examine here the maximum band velocity v_{max} in zigzag CNTs:

$$v_{max} = \frac{1}{\hbar}\left(\frac{dE}{dk}\right)\Big|_{max,\,b}\,. \tag{3.6}$$

The energy (E)-wavevector (k) relationship in sub-band b of a zig-zag tube of chiral index (n,0) can be expressed from Tight-binding theory [14]:

$$E = \gamma\left[1 + 4\cos(\frac{3ak}{2})\cos(\frac{\pi p}{n}) + 4cos^2(\frac{\pi p}{n})\right]^{0.5}\,, \tag{3.7}$$

where k is the longitudinal wavevector, $a = 0.142\,\text{nm}$ is the carbon-carbon bond length, p is an integer from 1 to $2n$ indicating the different bands, and γ is the overlap parameter.

From Eqns. (B.5) and (3.7), v_{max} in the first sub-band, and the energy E_a at which it is achieved, can be expressed as [13]:

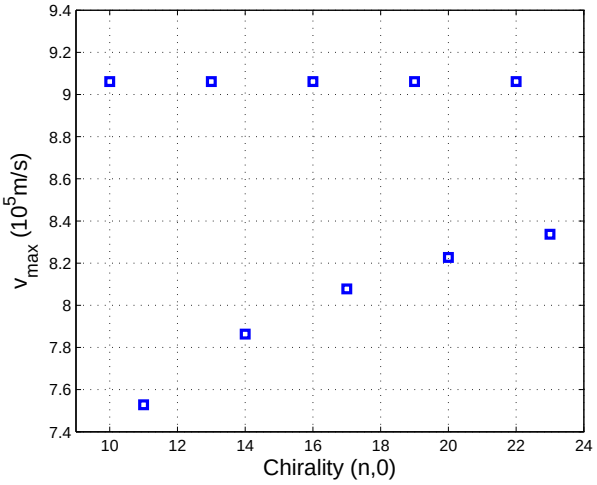

Figure 3.1: Dependence of maximum, band-structure limited velocity on chirality for zig-zag nanotubes.

For (3i+1,0) tube, $v_{max} = \frac{3a}{2\hbar}\gamma$, $E_a = \gamma\sqrt{4\cos^2(\frac{2i+1}{3i+1}\pi) - 1}$.

For (3i+2,0) tube, $v_{max} = -\frac{3a}{\hbar}\gamma\cos(\frac{2i+1}{3i+2}\pi)$, $E_a = \gamma\sqrt{1 - 4\cos^2(\frac{2i+1}{3i+2}\pi)}$.

Where i is an integer. v_{max} in the first band for zig-zag nanotubes $(n, 0)$ is drawn in Fig. 3.1. It can be seen that $v_{max} = 9.1 \times 10^5\,\mathrm{ms}^{-1}$ for tubes of chirality (3i+1,0), and that the maximum value for (3i+2,0) tubes increases towards this peak as the chiral index increases.

3.3 Results and Discussion

Simulation results are presented for coaxial, doped-contact CNFETs made from (22,0) nanotubes. In all cases, the gate length is 16 nm (to avoid direct source-drain tunneling [5]), the gate thickness is 1nm, the oxide thickness is 3.2 nm, the oxide relative permittivity is 3.9, and the source and drain lengths are 50 nm. The source and drain contact doping densities are $0.5\,\mathrm{nm}^{-1}$ for both the n- and p- type regions of the n-i-n and p-i-n CNFETs

that are to be compared. These specifications are similar to those for devices used in a study of switching performance [5], with the notable exception of the relative permittivity of the gate dielectric: we use 3.9, as opposed to the value of 16 used in [5], as this reduces the intrinsic capacitances, thereby improving f_T [12].

Figure 3.2 compares the band-determined velocity dispersion relationship from the two effective-mass models with that calculated from a Tight-binding, nearest-neighbor calculation using $\gamma = 2.8\,\mathrm{eV}$. It can be seen that an energy-dependent effective mass approach is necessary if the velocity is to be correctly modeled at energies above about 0.1 eV. As V_{DS} is increased, electrons will attain and exceed this energy on entering the drain. Thus, use of the constant-effective mass model will overestimate the velocity in this region, leading to an underestimate of the signal delay time in the drain [11], and, consequently, to an over-optimistic value of f_T. This fact is demonstrated in Fig. 3.3. The effect is more severe in the *p-i-n* case because of the opening-up of another high-energy current path at large V_{DS}, as illustrated in Fig. 3.4a. Specifically, at high bias, tunneling of electrons into the drain at energies close to that of the conduction-band edge in the drain is facilitated. This phenomena can also be viewed as tunneling of holes into the *i*-region. The holes enter this region at high energy, so their velocity is overestimated by the constant-effective-mass model. BTBT can also occur at high bias in *n-i-n* structures, as can be seen from the emergence of a subsidiary peak in the current spectrum in Fig. 3.4b. The onset of this current at $V_{GS} = 0.4\,\mathrm{V}$ is illustrated in Fig. 3.5. However, in this case, the holes injected into the *i*-region cause a charge build-up that, evidently, more severely affects f_T than does the increase in current, leading to a reduction in f_T ($= \frac{1}{2\pi}\frac{\Delta I}{\Delta Q}$). This is clear from Fig. 3.6, and is also shown in Fig. 3.3. The ambipolar nature of conduction in *p-i-n* CNFETs is well known [4, 5], and its effect on the gate characteristic is illustrated in Fig. 3.7. Contrarily, the *n-i-n* device shows the more usual, unipolar relationship. The ambipolarity necessitates the re-definition of f_T as $f_T = \frac{1}{2\pi}\left|\frac{\Delta I}{\Delta Q}\right|$ for the *p-i-n* case, with the result that f_T drops dramatically around the point of the current minimum (see Fig. 3.8), which occurs in this case at $V_{GS} = V_{DS}/2 = 0.2\,\mathrm{V}$. The different energy paths for the majority carriers (electrons at $V_{GS} > 0.2\,\mathrm{V}$, and holes at $V_{GS} < 0.2\,\mathrm{V}$), are evident in the diagrams of Figs. 3.9 and 3.10, respectively.

We now turn to the chirality-dependence of the maximum band-determined velocity v_{max}. The results are shown in Fig. 3.1, and the effect on f_T is shown in Fig. 3.11. For both the

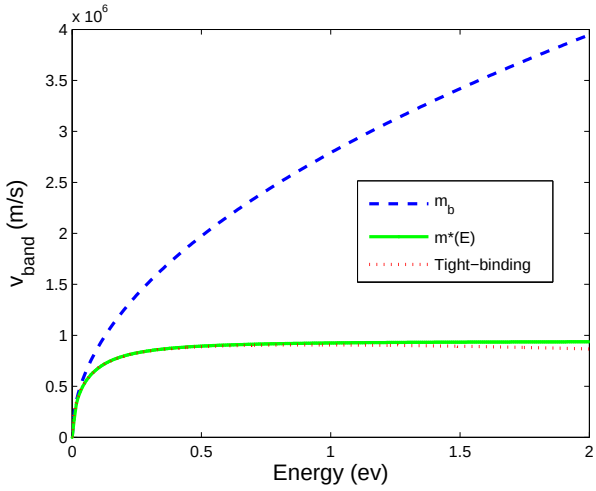

Figure 3.2: Energy dependence of v_{band}, as computed from a Tight-binding calculation (dotted line), and Hamiltonians using either an energy-dependent effective mass (solid line), or a constant effective mass (dashed line). Results are for the first sub-band of a (22,0) tube.

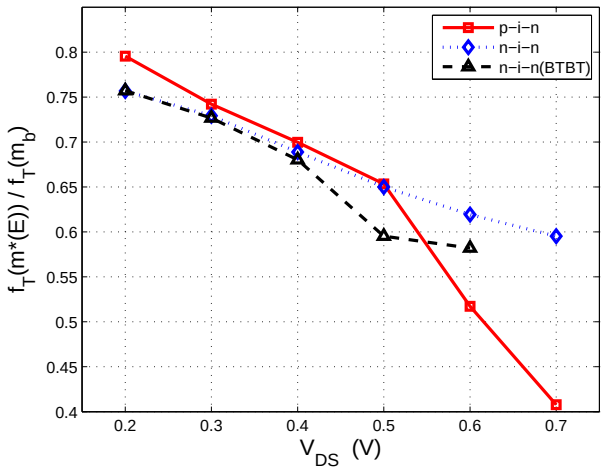

Figure 3.3: Drain-bias dependence at $V_{GS} = 0.4\,\mathrm{V}$ of the ratio of f_T for the EEM case to that for the CEM case. The effect of including BTBT in the *n-i-n* device is also shown.

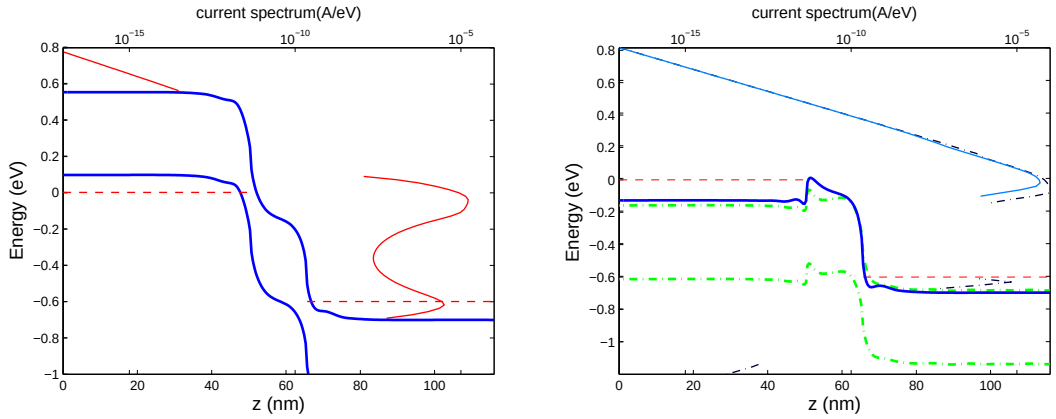

(a) (b)

Figure 3.4: Energy band diagams at V_{GS}=0.4 V and V_{DS}=0.6 V for doped-contact CNFETs: *p-i-n* (left), *n-i-n* (right). On the right, the thick dot-dashed lines are band edges when BTBT is included. The current spectrum in this case is shown by the thin dot-dashed lines. In both diagrams the dashed lines are the quasi-fermi levels in the contacts.

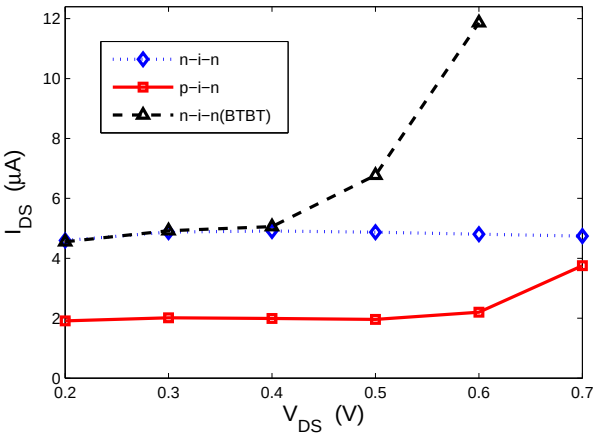

Figure 3.5: Comparison of the drain characteristics at V_{GS}=0.4 V.

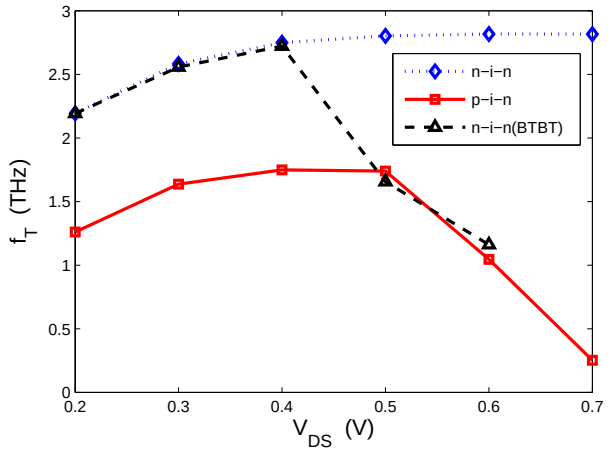

Figure 3.6: Comparison of the drain-bias dependence of f_T at V_{GS}=0.4 V.

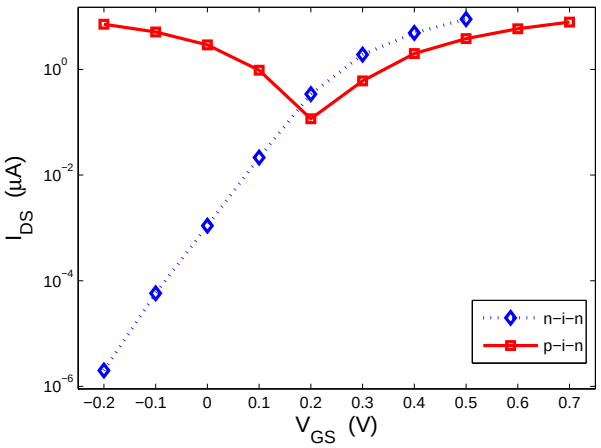

Figure 3.7: Comparison of the gate characteristics at $V_{DS} = 0.4$ V.

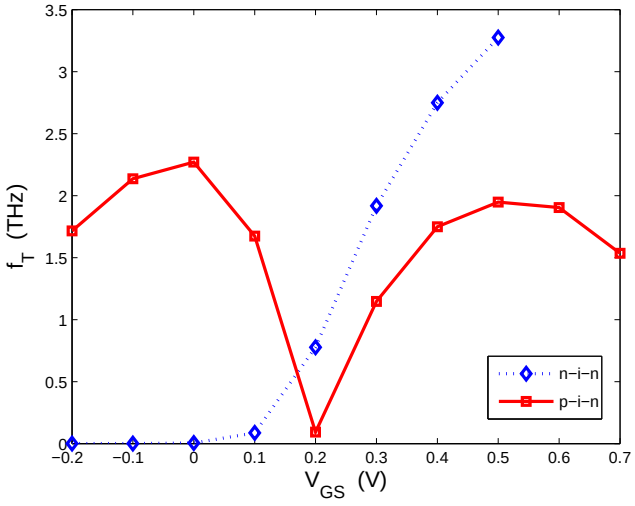

Figure 3.8: Comparison of the gate-bias dependence of f_T at $V_{DS} = 0.4\,\mathrm{V}$

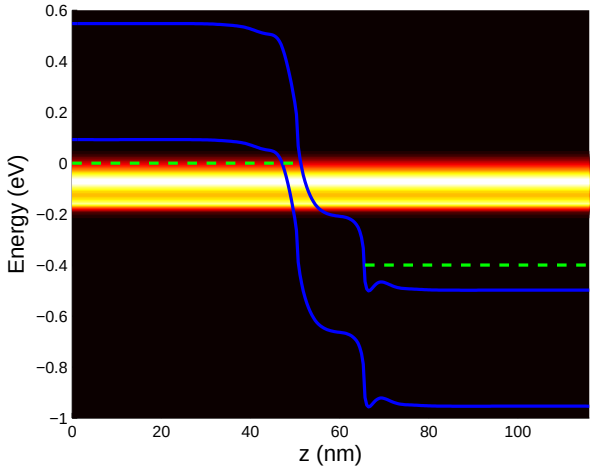

Figure 3.9: Current-energy spectrum for the *p-i-n* CNFET at V_{GS}=0.5 V, V_{DS} =0.4 V. The dashed lines are the Fermi levels in the doped contacts, and the solid lines are the band edges.

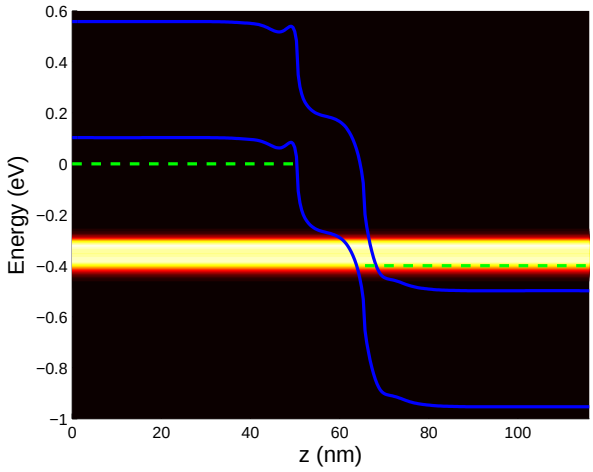

Figure 3.10: Current-energy spectrum for the *p-i-n* CNFET at V_{GS}=0 V, V_{DS} =0.4 V.

n-i-n and *p-i-n* devices the "oscillation" in v_{max} is manifest in f_T, but is superimposed on a steadily increasing value of f_T with chirality. In *n-i-n* devices, the increasing trend is due to a reduction of the source/channel barrier height with the lower bandgap that is associated with an increase in chirality [12]. In the *p-i-n* case, the lower bandgap leads to a thinner barrier for BTBT (see Fig. 3.12). In each case there is an increase in transconductance with chirality.

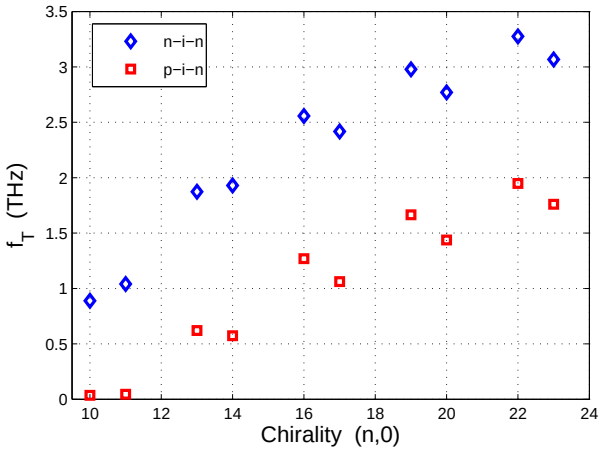

Figure 3.11: f_T dependence on chirality for n-i-n and p-i-n CNFETs. $V_{GS} = 0.5\,\mathrm{V}$, $V_{DS} = 0.4\,\mathrm{V}$.

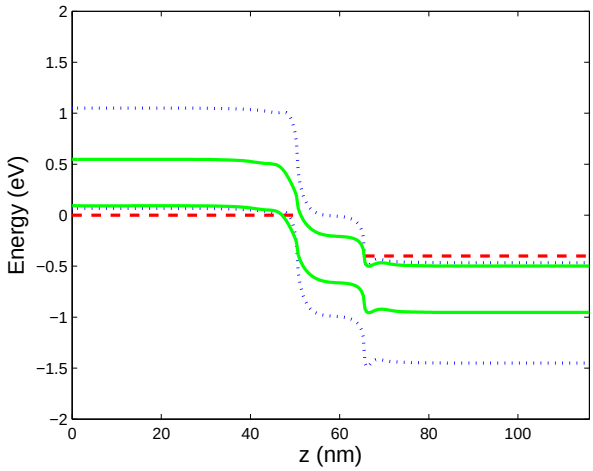

Figure 3.12: Energy band diagrams at V_{GS}=0.5 V and V_{DS}=0.4 V for *p-i-n* CNFETs made from tubes of chirality (10,0) (dotted lines) and (22,0) (solid lines). The dashed lines are the Fermi energies in the contacts.

3.4 Conclusion

From this simulation study of doped-contact CNFETs it can be concluded that:

- Use of an energy-dependent effective-mass model gives less optimistic predictions for f_T in both *p-i-n* and *n-i-n* CNFETs than does the usual, constant-effective-mass model.
- The high-frequency performance of both *n-i-n* and *p-i-n* CNFETs employing zig-zag tubes improves with chirality.
- Operation of *n-i-n* CNFETs at high drain bias may lead to reduced high-frequency performance due to charge build-up in the device as a result of BTBT.

References

[1] J. Knoch, *et al.* "One-Dimensional Nanoelectroinc Devices–Towards the Quantum Capacitance Limit", 66th Device Research Conference, pp. 173-176, Santa Barbara, USA, June 2008.

[2] J. Appenzeller, *et al.* "Comparing Carbon Nanotube Transistors–The Ideal Choice: A Novel Tunneling Device Design", IEEE Transactions on Electron Devices, vol. 52, issue 12, pp. 2568-2576, 2005.

[3] J. Appenzeller, Y.-M. Lin, J. Knoch and Ph. Avouris, "Band-to-Band Tunneling in Carbon Nanotube Field-Effect Transistors", Phys. Rev. Lett., vol. 93, no. 19, 196805, Nov. 2004.

[4] S.O. Koswatta, D.E. Nikonov and M.S. Lundstrom, "Computational study of carbon nanotube pin-tunnel FETs", IEDM Tech Dig, pp. 525-528, 2005.

[5] S. Poli, S. Reggiani, A. Gnudi, E. Gnani, and G. Baccarani, "Computational study of the ultimate scaling limits of CNT tunneling devices", IEEE Transactions on Electron Devices, vol. 55, pp. 313-321, 2008.

[6] Kathy Boucart and Adrian M. Ionescu, "Threshold voltage in Tunnel FETs: physical definition, extraction, scaling and impact on IC design", 37th European Solid-State Device Research Conference, pp. 299-302, Montreux, Switzerland, September 2006.

[7] D.L. John, L.C. Castro, P.J.S. Pereira, and D.L. Pulfrey, "A Schrödinger-Poisson solver for modeling carbon nanotube FETs", Tech. Proc. NSTI Nanotechnology Conf. and Trade Show, vol. 3, 65-68, Boston, 2004.

[8] Li Chen and D.L. Pulfrey, "Is there an Opportunity for Carbon Nanotube FETs in Very-High-Frequency Applications?", 66th Device Research Conference, pp. 111-112, Santa Barbara, USA, June 2008.

[9] H. Flietner, "The E(k) relation for a two-band scheme of semiconductors and the application to the metal-semiconductor contact", Phys. Stat. Sol. (b), vol. 54, 201-208, 1972.

[10] David Yuk Kei Ko and J. C. Inkson, "Matrix method for tunneling in heterostructures: Resonant tunneling in multilayer systems", Phys. Rev. B, vol. 38, 9945-9951, 1988.

[11] D.L. Pulfrey, L.C. Castro, D.L John, and M. Vaidyanathan, "Regional signal-delay analysis applied to high-frequency carbon nanotube FETs", IEEE Transactions on Nanotechnology. vol. 6, 711-717, 2007.

[12] D.L. Pulfrey and Li Chen, "Examination of the high-frequency capability of carbon nanotube FETs", Solid-State Electronics, accepted for publication, Feb. 22, 2008.

[13] Li Chen, "High-frequency limits of carbon nanotube transistors", M.A.Sc. thesis, The University of British Columbia, 2008.

[14] M P Anantram and F Léonard, "Physics of carbon nanotube electronic devices", 2006 Rep. Prog. Phys. 69, 507-561.

Chapter 4

Summary, Conclusions and Further Work

The semiconductor industry continues to scale metal-oxide-semiconductor transistors (MOSFETs), maintaining the predictions of Moores Law. Many physical restrictions are becoming more apparent and difficult to surpass with this aggressive scaling, such as drain induced barrier lowering (DIBL) and gate oxide leakage current. Carbon nanotube field-effect transistors (CNFETs) are being considered as one of the future electronic technologies because of their excellent performance. The variable band gap, depending on the chirality and CNT diameter, gives rise to nanotube properties ranging from metallic to semi-metallic to semiconducting. The work presented in this thesis displays their potential and limitations for high-frequency performance. From the simulation study of the effect of an energy-dependent effective mass model, we find the estimates for the band-structure-determined velocity are much superior to those using a constant effective-mass model, particularly at high energies; this superiority shows itself as the drain-source bias is increased, and indicates that estimates of f_{T} using a constant effective mass can be in large error.

In Chapter 2, new results are added to a recent critique of the high-frequency performance of carbon nanotube field-effect transistors. From a materials standpoint, carbon nanotubes are potentially good for high-frequency because of high band-structure-limited velocity, which reduces the channel charging time. The image-charge effects, which can lead to the signal velocity being higher than the propagation velocity (band-structure-limited velocity) in field regions of bipolar transis-

tors, are not significant in nanoscale FETs. The comparison between doped *n-i-n* and SB CNFETs shows the higher transconductance occurs in doped-contact CNFETs due to the reduced quantum-mechanical reflection of electrons at the injecting source/intrinsic-nanotube interface. From a device practical standpoint, however, CNFETs may be limited by parasitics associated with gate-metal thickness and contact resistance.

The constant-effective-mass model (CEM) used here gives optimistic predictions for f_{T} especially at high drain-source bias. When electrons are injected into the drain reservoir with high energy, the propagation velocity should be lower than the value deducted from the parabolic band structure from CEM. This case has been explicitly explained in Chapter 3. Its impact on both *n-i-n* and *p-i-n* doped-contact CNFETs is explored and compared. Band-to-band tunneling (BTBT), which occurs in traditional devices such as Zener diodes, can apparently be exploited to build nano-scale *p-i-n* transistors for low-power applications. This effect shows its ambipolar nature in *p-i-n* transistors and also reduces f_{T} in *n-i-n* CNFETs due to charge build-up in the device as a result of BTBT. For zig-zag tubes, the propagation velocity has a maximum value (for the first sub-band) of $v_{b,max} = 9.1 \times 10^5$ m/s for tubes of chirality (3i+1,0), where i is an integer, and a peak value that increases towards $v_{b,max}$ as i increases for tubes of chirality (3i+2,0). When this oscillation in peak velocity is combined with the improvement in g_m for both *n-i-n* and *p-i-n* CNFETs, f_{T} also oscillates with the chiral index increase of zig-zag tubes for both devices.

In conclusion, this study of the high-frequency performance of carbon nanotube FETs has shown that:

1. A constant-effective mass model can lead to large overestimates of f_{T}. This error can be greatly reduced by using the energy-dependent effective-mass model developed in this thesis.

2. Incorporation of an energy-dependent effective-mass model into our Schrödinger-Poisson solver allows band-to-band tunneling to be investigated. This transport

mechanism is the main conduction process in *p-i-n* CNFETs, but it also exists in *n-i-n* CNFETs, where it can reduce f_{T} due to charge build-up in the channel.

3. Inclusion of parasitics, particularly gate-source and gate-drain capacitance due to having practical values of gate-metal thickness, can seriously reduce f_{T}. The reduction may be so severe that CNFETs will not realize the advantage they have over other transistors due to their superior intrinsic properties.

During the course of implementing BTBT into our SP solver, the question of what value to use for the energy level that distinguishes electrons from holes arose. Issues connected with this are summarized in Appendix C, which will hopefully be of use to someone wishing to study the effect in more detail.

Appendix A

Matrix Method for Heterostructure Transport

This appendix describes solving the schrödinger equation for the carrier transport in the heterostructure.

A.1 Scatter Matrix

In figure A.1, for a finite N+1 layer structure, **a** and **b** are the coefficients of the "forward" and the "backward" states, respectively. As explained in [1], the forward states are defined as waves which propagate or exponentially decay in the positive-z direction, and the backward states behave similarly, but in the negative-z direction. The relationship for the transfer matrix from layer **0** to **N** is:

$$\begin{bmatrix} a_0 \\ b_0 \end{bmatrix} = T(0,N) \begin{bmatrix} a_N \\ b_N \end{bmatrix}. \tag{A.1}$$

The equivalent scatter matrix $S(0,N)$ would be:

$$\begin{bmatrix} a_N \\ b_0 \end{bmatrix} = S(0,N) \begin{bmatrix} a_0 \\ b_N \end{bmatrix}. \tag{A.2}$$

Figure A.1: Tunneling in multilayer system

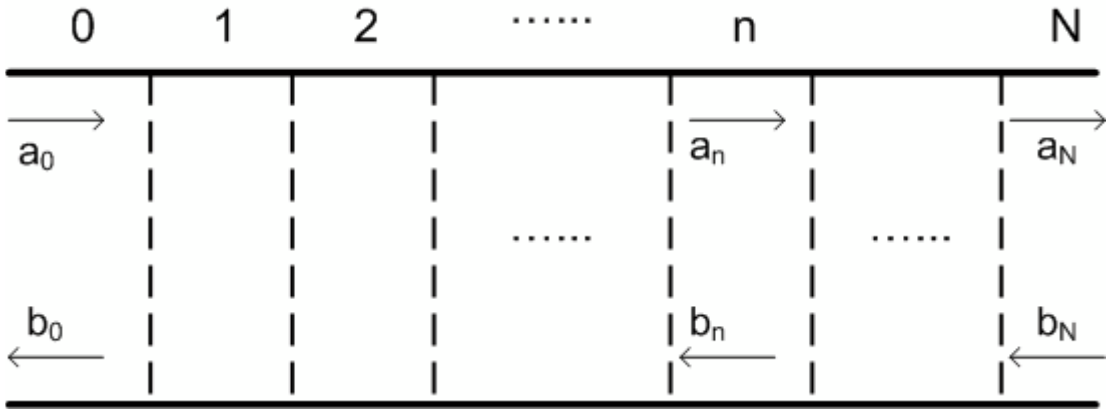

The matching conditions for the (n+1)th interface can be expressed below [2]:

$$\begin{bmatrix} a_n \\ b_n \end{bmatrix} = K(n+1) \begin{bmatrix} a_{n+1} \\ b_{n+1} \end{bmatrix}. \tag{A.3}$$

The details of the construction of the K interfacial matrix are given in the literature [2], and will be demonstrated for our specific case in the next section.

For simplicity, the **S** matrices and the **K** represent $S(0,n)$ and $K(n+1)$, respectively. Assume a semi-infinite boundary condition and a wave that propagates from left to right, then set $a_0 = 1$, $b_N = 0$. Combined with the deduction in [1], the coefficients are given by:

$$\begin{cases} a_n = [1 - S_{12}(0,n)S_{21}(n,N)]^{-1} S_{11}(0,n) \\ b_n = [1 - S_{21}(n,N)S_{12}(0,n)]^{-1} S_{21}(n,N)S_{11}(0,n) \end{cases}. \tag{A.4}$$

In the above equations, $S_{11}(0,n)$, $S_{12}(0,n)$ could be solved through iteration starting from the first layer [1]:

$$\begin{cases} S_{11}(0,n+1) = S_{11}(K_{11} - S_{12}K_{21})^{-1} \\ S_{12}(0,n+1) = S_{11}(0,n+1)(S_{12}K_{22} - K_{12})S_{11}^{-1} \end{cases} . \tag{A.5}$$

The remaining problem is to find an expression for $S_{21}(n,N)$ expression as follows.

First we define matrix K':

$$\begin{bmatrix} b_{n+1} \\ a_{n+1} \end{bmatrix} = K'(n+1) \begin{bmatrix} b_n \\ a_n \end{bmatrix}, \tag{A.6}$$

and matrix $I = K^{-1}$.

It's easy to prove $I_{ii} = K'_{jj}$, $I_{ij} = K'_{ji}$ and $S_{ii}(n,N) = S_{jj}(N,n)$; where $i,\ j = 1,2$ and $i \neq j$.

Use the relations above and equations (A.5)

$$\begin{aligned} S_{21}(n,N) &= S_{12}(N,n) \\ &= S_{11}(N,n)[S_{12}(N,n+1)K'_{22} - K'_{12})]S(N,n+1) \\ &= [S_{21}(n+1,N)K'_{22} - K'_{12}][K'_{11} - S_{21}(n+1,N)K'_{21}]^{-1} \\ &= [S_{21}(n+1,N)I_{11} - I_{21}][I_{22} - S_{21}(n+1,N)I_{12}]^{-1}. \end{aligned} \tag{A.7}$$

Therefore coefficients in (A.4) can be solved by equations (A.5) and (A.7). The approach hereinabove only requires initial boundary conditions $\mathbf{a_0}$ and $\mathbf{b_N}$, hence the errors in the coefficients do not propagate from one layer to the next.

A.2 Interface Matrix

In figure A.1, define $\mathbf{a_n}$, $\mathbf{b_n}$ as the wavefunction coefficients of the beginning point of layer n; $\mathbf{a'_n}$, $\mathbf{b'_n}$ are coefficients at the end point of layer n. Assuming the coordinate of interface between layer n and $n+1$ is zero, the wavefunctions within layers n and $n+1$ can be expressed as:

$$\psi(z) = \begin{cases} a'_n e^{ik_n z} + b'_n e^{ik_n z} & z < 0 \\ a_{n+1} e^{ik_{n+1} z} + b_{n+1} e^{ik_{n+1} z} & z > 0, \end{cases} \tag{A.8}$$

where k_n is the wavevector in layer n. From quantum mechanic of boundary conditions:

$$\begin{cases} a'_n + b'_n = a_{n+1} + b_{n+1} \\ (a'_n k_n - b'_n k_n) m_n^{-1} = (a_{n+1} k_{n+1} - b_{n+1} k_{n+1}) m_{n+1}^{-1}, \end{cases} \tag{A.9}$$

where m_n is the effective mass in layer n; a_n and a'_n are in the same layer with interval length d, therefore $a'_n = a_n e^{ik_n d}$, $b'_n = b_n e^{-ik_n d}$. Written in matrix form:

$$\begin{bmatrix} a_{n+1} \\ b_{n+1} \end{bmatrix} = 0.5 \begin{bmatrix} 1+\alpha & 1-\alpha \\ 1-\alpha & 1+\alpha \end{bmatrix} \begin{bmatrix} e^{ik_n d} & 0 \\ 0 & e^{-ik_n d} \end{bmatrix} \begin{bmatrix} a_n \\ b_n \end{bmatrix} \tag{A.10}$$

$$= I \begin{bmatrix} a_n \\ b_n \end{bmatrix}, \tag{A.11}$$

where $\alpha = \frac{k_n m_{n+1}}{k_{n+1} m_n}$ and $I = K^{-1}$.

The advantage of using (A.10) is that the probability in each layer can be expressed as the "sum of coefficients": $|\psi_n|^2 = |a_n + b_n|^2$.

References

[1] David Yuk Kei Ko and J. C. Inkson, "Matrix method for tunneling in heterostructures: Resonant tunneling in multilayer systems", *Phys. Rev. B*, 38(14), 9945-9951 (1988).

[2] A.C. Marsh and J. C. Inkson, "Scattering matrix theory of transport in heterostructures", Semicond. Sci. Technol. 1, 285-290 (1986).

Appendix B

Zigzag CNT Band Velocity

In this appendix, the maximum first sub-band-determined velocity for zigzag carbon nanotubes is derived from the Tight-Binding approximation.

B.1 Maximum Band Velocity

From [1], for zigzag tube $(n, 0)$, the E-k relationship for conduction band is:

$$E = \gamma[1 + 4\cos(\frac{3ak}{2})\cos(\frac{\pi p}{n}) + 4cos^2(\frac{\pi p}{n})]^{0.5}. \tag{B.1}$$

Here, k is the longitudinal wavevector and $k \in [0, \frac{\pi}{3a}]$, $a = 0.142\,\text{nm}$ is the carbon-carbon bond length, p is an integer from 1 to $2n$, and γ is the overlap parameter.[1]

Equation (B.1) yields the band velocity:

$$v = \frac{1}{\hbar}\frac{dE}{dk} = \frac{-\gamma^2}{\hbar}\frac{3a\cos(\frac{\pi p}{n})\sin(\frac{3ak}{2})}{E}, \tag{B.2}$$

[1]Here, γ=2.8 eV.

where $\hbar$ is Dirac constant.[2] Define E_a and k_a as the corresponding band energy and wave vector, respectively, to achieve the maximum velocity v_{max}, where the derivative of v with respect to k is zero:

$$\frac{dv}{dk}\Big|_{k=k_a} = 0.$$

This renders $\frac{3a}{2}\cos(\frac{3ak_a}{2})E_a - \sin(\frac{3ak_a}{2})\frac{dE}{dk}\Big|_{k=k_a} = 0.$

Utilize the definition of velocity $v = \frac{1}{\hbar}\frac{dE}{dk}$, v_{max} is given by:

$$v_{max} = \frac{3a}{2\hbar}\cot(\frac{3ak_a}{2})E_a, \tag{B.3}$$

$$E_a = \gamma\sin(\frac{3ak_a}{2})[\frac{-2\cos(\frac{\pi p}{n})}{\cos(\frac{3ak_a}{2})}]^{0.5}. \tag{B.4}$$

Eliminate E_a, v_{max} can be expressed as:

$$v_{max} = \frac{3a}{2\hbar}\gamma\sqrt{-2c\cos(\frac{3ak_a}{2})}. \tag{B.5}$$

Where $c = \cos(\frac{\pi p}{n})$ and the c, k relation is written as:

$$\cos(\frac{3ak_a}{2}) = \frac{-4c^2 - 1 \pm |4c^2 - 1|}{4c}. \tag{B.6}$$

[2] $\hbar = 1.0546 \times 10^{-34}\, J \cdot s.$

B.2 The First Sub-band v_{max}

The lowest energy for each sub-band occurs when $k = 0$. Hence from (B.1):

$$E = \gamma \left| 1 + 2\cos(\frac{\pi p}{n}) \right|. \tag{B.7}$$

Obviously, for the first sub-band, p is an integer to satisfy: $\cos(\frac{\pi p}{n}) \longrightarrow -0.5$. With the constraint $p = 1, 2, ...2n$, then $p \rightarrow 2n/3$ or $4n/3$. Considering $p \longrightarrow 4n/3$ as a degenerate band, this also indicates the degeneracy of the zigzag CNT first sub-band is always 2.

c is negative for the first sub-band, from (B.6), $\cos(\frac{3ak_a}{2}) = \begin{cases} -1/(2c); & -1 < c \leqslant -0.5 \\ -2c; & -0.5 \leq c < 0 \end{cases}$.
Substituting into (B.5):

$$v_{max} = \frac{3a}{2\hbar}\gamma \begin{cases} 1, & -1 < c \leqslant -0.5 \\ -2c, & -0.5 \leq c < 0. \end{cases} \tag{B.8}$$

The equation above indicates that the first band maximum velocity for semiconductor zigzag tube is $9.0609 \times 10^5\, m/s$. Through further investigation, this maximum velocity is divided into two categories for different zigzag tubes. One is $(3i + 1, 0)$, the "first class" of tube with i as an integer. For these tubes, v_{max} is constant. The other one is the $(3i + 2, 0)$ tube for which the v_{max} is smaller than the previous class and will go close to the "first class" v_{max} when i increases. Details of the proof are in the next section.

B.3 Choice of Parameter p

From (B.7), the first sub-band half-band gap E_1 satisfies:

$$\frac{E_1}{\gamma} = \begin{cases} 1 + 2\cos(\frac{\pi p}{n}), & \cos(\frac{\pi p}{n}) > -0.5 \\ -1 - 2\cos(\frac{\pi p}{n}), & \cos(\frac{\pi p}{n}) < -0.5. \end{cases} \tag{B.9}$$

Lemma1: For $(3i+1, 0)$ and $(3i+2, 0)$ tubes, p for the first sub-band satisfies $\cos(\frac{\pi p}{n}) < -0.5$ and $\cos(\frac{\pi p}{n}) > -0.5$, respectively.

Proof: **For** $(3i+1, 0)$ tube, as mentioned before, $\cos(\frac{\pi p}{n}) \longrightarrow -0.5$ to attain minimum E_1. It's quickly to pick p either $2i$ or $2i+1$ and yield the following expression:

$$\frac{\pi p}{n} - \frac{2\pi}{3} = \triangle y = \begin{cases} -2\triangle x, & p = 2i \\ \triangle x, & p = 2i+1, \end{cases} \text{ where } \triangle x = \frac{\pi}{3}\frac{1}{3i+1}.$$

Substitute $\frac{\pi p}{n} = \triangle y + \frac{2\pi}{3}$ into (B.9), And the statement that $\cos(\frac{\pi p}{n}) < -0.5$ to attain minimum E_1 is equal to the inequality below:

$$1 + \cos(\frac{2\pi}{3} - 2\triangle x) + \cos(\frac{2\pi}{3} + \triangle x) > 0.$$

Starting from the left hand side and using the inequality [3] $\cos(\frac{2\pi}{3} - 2\triangle x) > \cos(\frac{2\pi}{3} - \triangle x)$:

$$\begin{aligned} LHS &> 1 + \cos(\frac{2\pi}{3} - \triangle x) + \cos(\frac{2\pi}{3} + \triangle x)\,\mathrm{dd} \\ &= 1 + 2\cos(\frac{2\pi}{3})\cos(\triangle x) \\ &= 1 - \cos(\triangle x) > 0. \end{aligned}$$

This proves the statment for a $(3i+1, 0)$ tube.

[3] From $\triangle x$ expression $\frac{\pi}{3}\frac{1}{3i+1}$, when $i = 0$, $\triangle x = \frac{\pi}{3}$, thus $\triangle x \leq \frac{\pi}{3}$ and both $\frac{2\pi}{3} - \triangle x$, $\frac{2\pi}{3} - 2\triangle x$ stay in the same range where the cosine function is monotonically decreasing.

For $(3i+2,0)$ tube**,** similarly, it's equivalent to prove the inequality below:

$$1+\cos(\frac{2\pi}{3}-\triangle x)+\cos(\frac{2\pi}{3}+2\triangle x)<0,$$

with $\triangle x=\frac{\pi}{3}\frac{1}{3i+2}$ and $p=2i+1$ or $2i+2$. Using "Sum to product" to change the left hand side:

$$LHS \quad = \quad 1+2\cos(\frac{2\pi}{3}+\frac{\triangle x}{2})\cos(\frac{3\triangle x}{2})$$

Obviously, $\triangle x \leqslant \frac{\pi}{6}$. Hence LHS is a monotonic decreasing function with respect to $\triangle x$, and $LHS \longrightarrow 0$ when $\triangle\ x \longrightarrow 0$. Thus the result follows.

B.4 Conclusion

From the discussion above, v_{max} and the energy E_a to achieve v_{max} in the first sub-band can be expressed as:

For $(3i+1,0)$ tube, $p=2i+1$, $v_{max}=\frac{3a}{2\hbar}\gamma$, $E_a=\gamma\sqrt{4\cos^2(\frac{2i+1}{3i+1}\pi)-1}$;

For $(3i+2,0)$ tube, $p=2i+1$, $v_{max}=-\frac{3a}{\hbar}\gamma\cos(\frac{2i+1}{3i+2}\pi)$, $E_a=\gamma\sqrt{1-4\cos^2(\frac{2i+1}{3i+2}\pi)}$.

References

[1] M P Anantram and F Léonard, "Physics of carbon nanotube electronic devices", Rep. Prog. Phys. 69, 507-561 (2006).

Appendix C

Issues of Band-to-band Tunneling in CNFETs (BTBT)

In this appendix, the problem in modeling BTBT has been provided and is the topic for future work.

C.1 Modeling without Band to Band Tunneling

The wavevector $k = k(E, z)$ is given by:

$$k^2 = \begin{cases} \frac{2m_b}{\hbar^2}(E - E_0 - \triangle_b), & \text{for electrons} \\ \frac{2m_b}{\hbar^2}(-E + E_0 - \triangle_b), & \text{for holes,} \end{cases} \tag{C.1}$$

where E_0 is the midgap energy, $\triangle_b$ is the energy distance between the bottom of sub-band b and E_0, and m_b is the effective mass for sub-band b.

From the specified band structure, we can compute $k(E, z)$ for electrons and holes separately.

We use the scatter matrix method in [1] to obtain the carrier wavefunction $\psi(E, z)$ propagating from either source or drain.

This is done by the function *scattmat* in our Schrödinger-Poisson (SP) solver:

[AS,BS,AD,BD]=scattmat(kS,kD,dz)

The input of this function are **kS, kD** the wavevectors from source and drain, respectively, and **dz** the length of each piece-wise rectangular barrier step. The outputs are coefficients of the wavefunctions from the source and drain. Both Ai and ki (i=**S**ource or **D**rain) have the same dimensions.

Take the source-originating charge for example, the carrier is an electron or a hole depending on whether the carrier energy level is larger than the source conduction band or smaller than the source valence band, respectively. The local density of states (ldos: $\mathcal{G}_s(E,z)$) from the source is expressed by [2]:

$$\mathcal{G}_s(E,z) = D_b g_s(E)\psi_s(E,z)\psi_s^*(E,z), \tag{C.2}$$

and

$$\psi_s(E,z)\psi_s^*(E,z) = |AS(E,z) + BS(E,z)|^2, \tag{C.3}$$

where D_b is the degeneracy of the sub-band b, $g_s(E)$ is the 1D non-local density of states in the neutral region of the source contact.

Therefore:

$$Qs(E,z) = \begin{cases} -q\mathcal{G}_s(E,z)f_s(E) & \text{for electrons,} \\ q\mathcal{G}_s(E,z)[1-f_s(E)] & \text{for holes.} \end{cases} \tag{C.4}$$

Similar expressions are used for charges originating in the drain contact.

C.2 Modeling with Band to Band Tunneling

The wavevector $k = k(E, z)$ is given by:

$$k^2 = \frac{2m_b}{\hbar^2}(|E - E_0| - \triangle_b). \tag{C.5}$$

Except for the wavevector formula, the ldos is computed in the same way as for the non-interband tunneling case.

The ldos $\mathcal{G}_s(E, z)$ near the source Fermi level injected from source is shown in Fig. C.1

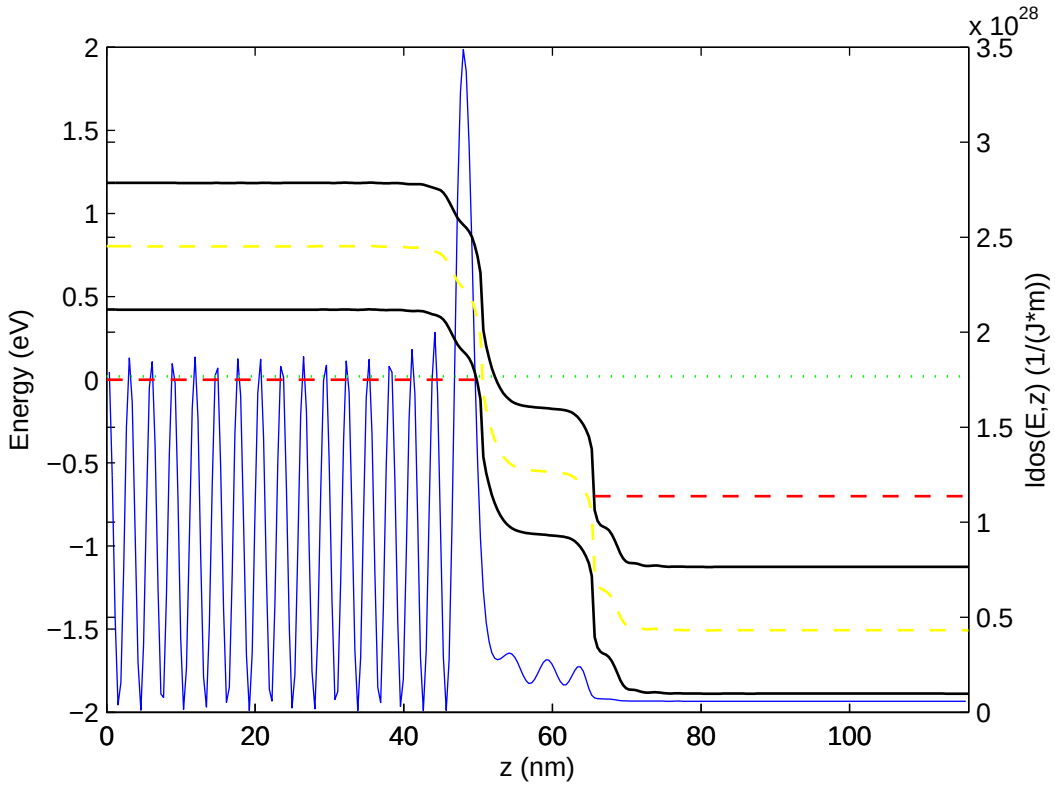

Figure C.1: *p-i-n* CNFET band structure, V_{GS}=0.6 V, V_{DS}=0.7 V. The gate length is 16 nm. The dotted horizontal line illustrates carriers interband tunnelling at energy 0.02 eV, the dashed line between the conduction and valence band is E_0 and the fluctuant solid line is ldos.

Another difference that arises with interband tunneling in the SP solver is how to calculate charge density. Take the source-originating charge Qs for example:

$$Qs(E,z) = q\mathcal{G}_s(E,z)[u(E,z) - f_s(E)] \tag{C.6}$$

The parameter u is used to differentiate between electrons and holes and the division level is set at E_0:

$$u(z,E) = \begin{cases} 0, & E > E_0 \quad \text{(electron)} \\ 1, & E < E_0 \quad \text{(hole).} \end{cases} \tag{C.7}$$

However the setting of the division line at the middle level of the band gap is still arbitrary. Further work needs to be done to arrive at a more rigorous definition for E_0. In the following we show how the placement of the dividing energy level can affect the charge calculations.

Figure C.2 is the simulation results using the same *p-i-n* CNFET made from (13,0) nanotubes described in [3]: the gate length is 16 nm, the oxide thickness is 3.2 nm, the oxide relative permittivity is 16 (HfO_2), the source and drain contact doping densities are $1.5 \times 10^9\,\mathrm{m}^{-1}$and the source and drain length 50 nm. The bias voltage $V_{GS} = 0.6\,\mathrm{V}$ and $V_{DS} = 0.4\,\mathrm{V}$. The left figure is setting the division level at E_0. When the level is shifted to the valence band edge, there will be more charges with negative sign (electrons). This is shown by the "dip" in the right figure.

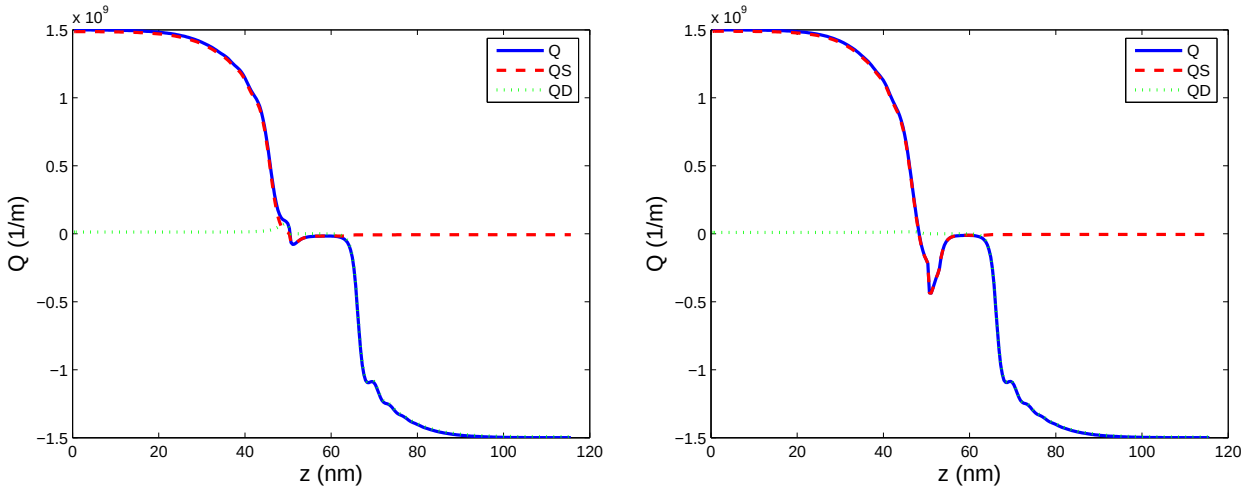

Figure C.2: The source- and drain-originating components of the spatial charge distribution. The total charge (solid line), Q_S (dashed line), Q_D (dotted line). The left figure is the result from equation (C.7) and the right is generated by moving the division line to the valence band edge.

C.3 *n-i-n* CNFET: with and without BTBT

The spatial change of the charge is shown in figure C.3 and C.4. The left and right figures are for no BTBT and for BTBT, respectively. In figure C.3, the device used here is the same to the reference [2] with $L_S = L_D = 30\,\text{nm}$, $L_G = 7\,\text{nm}$. The interband tunnelling only makes up a small portion of the current in this case. However, for a *n-i-n* CNFET with the same the configuration as in [4], with $L_S = L_D = 50\,\text{nm}$, $L_G = 16\,\text{nm}$, the interband tunnelling significantly changes the charge distribution and this effect is demonstrated in figure C.4.

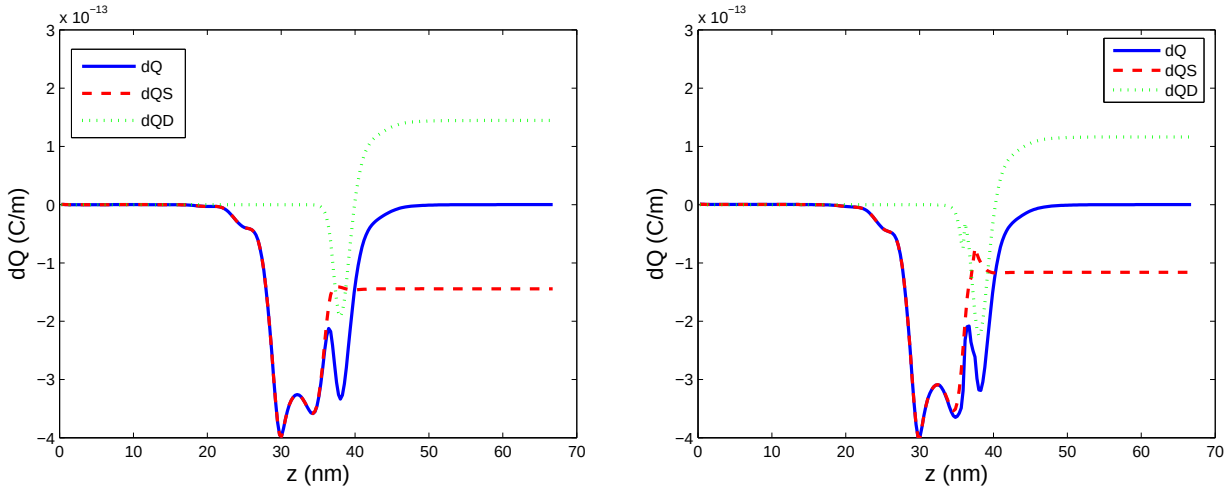

Figure C.3: Change in the source- and drain-originating components of the spatial charge for $\partial V_{GS} = +5\,\mathrm{mV}$ at $V_{GS} = V_{DS} = 0.7\,\mathrm{V}$. (11,0) CNFET, without (left) and with (right) interband tunnelling simulation.

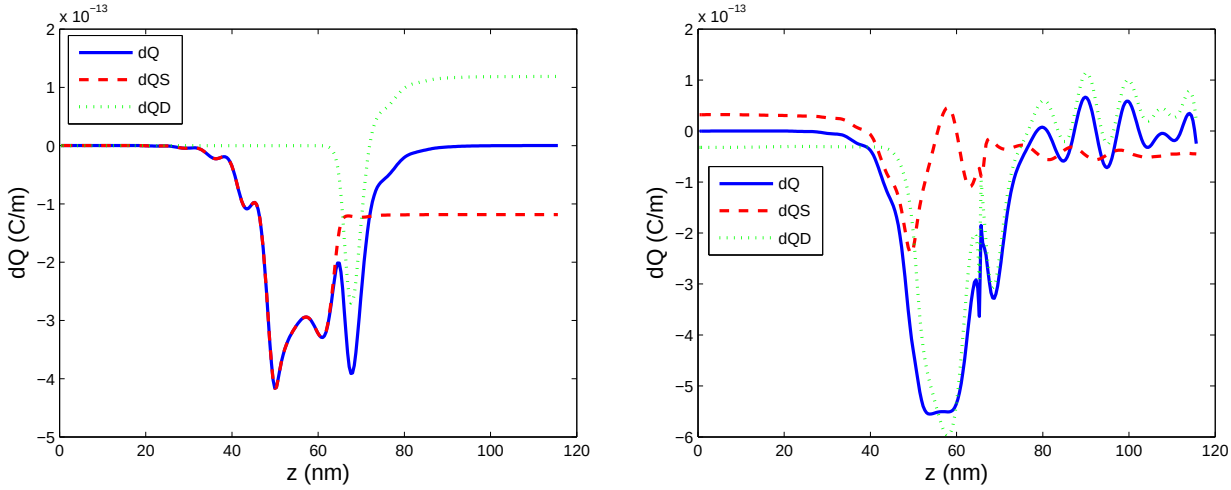

Figure C.4: Change in the source- and drain-originating components of the spatial charge for $\partial V_{GS} = +5\,\mathrm{mV}$ at $V_{GS} = 0.4\,V$, $V_{DS} = 0.6\,\mathrm{V}$. (22,0) CNFET, without (left) and with (right) interband tunnelling simulation.

References

[1] David Yuk Kei Ko and J. C. Inkson, "Matrix method for tunneling in heterostructures: Resonant tunneling in multilayer systems," Phys. Rev. B, 38(14), 9945-9951, 1988.

[2] D.L. Pulfrey, L.C. Castro, D.L John, and M. Vaidyanathan, "Regional signal-delay analysis applied to high-frequency carbon nanotube FETs", IEEE Trans. Nanotechnology. vol. 6, 711-717, 2007.

[3] S. Poli, S. Reggiani, A. Gnudi, E. Gnani, and G. Baccarani, "Computational study of the ultimate scaling limits of CNT tunneling devices", IEEE Transactions on Electron Devices, vol. 55, pp. 313-321, 2008.

[4] Li Chen and D.L. Pulfrey, "Comparison of p-i-n and n-i-n carbon nanotube FETs regarding high-frequency performance", Solid-State Electronics, submitted.